A MAGNIFIED VIEW OF THE KINEMATICS AND MORPHOLOGY OF RCSGA 032727-132609: ZOOMING IN ON A MERGER AT $z = 1.7$

EVA WUYTS[1], JANE R. RIGBY[2], MICHAEL D. GLADDERS[3,4], AND KEREN SHARON[5]
[1] Max-Planck-Institut für extraterrestrische Physik, Postfach 1312, Giessenbachstr., D-85741 Garching, Germany
[2] Observational Cosmology Lab, NASA Goddard Space Flight Center, Greenbelt, MD 20771, USA
[3] Department of Astronomy and Astrophysics, University of Chicago, 5640 South Ellis Avenue, Chicago, IL 60637, USA
[4] Kavli Institute for Cosmological Physics, University of Chicago, 5640 South Ellis Avenue, Chicago, IL 60637, USA
[5] Department of Astronomy and Astrophysics, University of Michigan, 500 Church Street, Ann Arbor, MI 48109, USA
Received 2013 August 21; accepted 2013 December 4; published 2014 January 8

ABSTRACT

We present a detailed analysis of multi-wavelength *Hubble Space Telescope*/Wide Field Camera 3 (WFC3) imaging and Keck/OSIRIS near-infrared adaptive optics-assisted integral field spectroscopy for a highly magnified lensed galaxy at $z = 1.70$. This young starburst is representative of ultraviolet-selected star-forming galaxies (SFGs) at $z \sim 2$ and contains multiple individual star-forming regions. Due to the lensing magnification, we can resolve spatial scales down to 100 pc in the source plane of the galaxy. The velocity field shows disturbed kinematics suggestive of an ongoing interaction and there is a clear signature of a tidal tail. We constrain the age, reddening, star formation rate, and stellar mass of the star-forming clumps from spectral energy distribution (SED) modeling of the WFC3 photometry and measure their Hα luminosity, metallicity, and outflow properties from the OSIRIS data. With strong star-formation-driven outflows in four clumps, RCSGA0327 is the first high-redshift SFG at stellar mass $<10^{10}\,M_\odot$ with spatially resolved stellar winds. We compare the Hα luminosities, sizes, and dispersions of the star-forming regions with other high-z clumps as well as local giant H II regions and find no evidence for increased clump star formation surface densities in interacting systems, unlike in the local universe. Spatially resolved SED modeling unveils an established stellar population at the location of the largest clump and a second mass concentration near the edge of the system that is not detected in Hα emission. This suggests a picture of an equal-mass mixed major merger, which has not triggered a new burst of star formation or caused a tidal tail in the gas-poor component.

Key words: galaxies: high-redshift – galaxies: kinematics and dynamics – galaxies: structure – gravitational lensing: strong

Online-only material: color figures

1. INTRODUCTION

High-redshift star-forming galaxies (SFGs) show increasingly irregular and clumpy morphologies compared with galaxies in the local universe. This was first observed at rest-frame ultraviolet (UV) wavelengths with the *Hubble Space Telescope* (*HST*; Griffiths et al. 1994; van den Bergh et al. 1996; Elmegreen et al. 2007) and has since been confirmed in rest-frame optical light (Elmegreen et al. 2009; Förster Schreiber et al. 2011; Guo et al. 2012), Hα emission (Swinbank et al. 2009; Jones et al. 2010; Genzel et al. 2011; Livermore et al. 2012; Wisnioski et al. 2012), and submillimeter emission (Swinbank et al. 2010). Locally, such irregular morphologies are associated with mergers, but a range of recent observational findings point toward this not being the common explanation at high redshift. The existence of a tight correlation between star-formation rate (SFR) and stellar mass out to at least $z \sim 2.5$, referred to as the main sequence of star formation, favors continuous star formation activity over a series of rapid, luminous merger-driven bursts (Noeske et al. 2007; Elbaz et al. 2007; Daddi et al. 2007; Wuyts et al. 2011). Outliers of the main sequence account for only 10% of the cosmic star formation density at $z \sim 2$ (Rodighiero et al. 2011). Counts of both galaxy pairs and disturbed morphologies (Conselice et al. 2009; Lotz et al. 2011; Kaviraj et al. 2013), as well as studies of gas-phase kinematics (Förster Schreiber et al. 2009; Epinat et al. 2012), limit the $z \sim 2$ merger rate to up to 30%. Based on the high gas fractions of 30%–80% (Daddi et al. 2010; Tacconi et al. 2010, 2013) and high velocity dispersions of 50–100 km s^{-1} (Förster Schreiber et al. 2009;

Law et al. 2009; Wisnioski et al. 2011) of $z \sim 2$ SFGs, an alternative picture has developed where luminous kiloparsec-sized clumps are formed through gravitational instabilities in a dynamically unstable, gas-rich, turbulent disk (Noguchi 1999; Immeli et al. 2004a, 2004b; Bournaud et al. 2007; Dekel et al. 2009; Genel et al. 2012). If they can survive long enough, these clumps are expected to migrate toward the center of the galaxy due to dynamical friction and coalesce into a young bulge on timescales of ∼0.5 Gyr. In this scenario, the galaxy's gas reservoir is continuously replenished by the accretion of gas from the halo through minor mergers and cold flows, to sustain the observed large gas fractions and strong star formation activity (Kereš et al. 2005, 2009; Bournaud & Elmegreen 2009; Dekel et al. 2009). These observational and theoretical results favor internal secular evolution over major mergers to explain the high star formation density and clumpy morphology of SFGs at $z \sim 2$. However, merging is still thought to play an important role in the cosmological mass assembly of galaxies, the quenching of star formation, and the morphological transitions of galaxies from late to early type (e.g., Springel et al. 2005; Naab & Burkert 2003; Naab et al. 2007; Guo & White 2008; Hopkins et al. 2010).

Current observational studies of the kinematics of high-z SFGs and the properties of their individual star-forming regions are limited by the available spatial resolution. At FWHM $\sim 0\farcs1$, which corresponds to roughly 1 kpc at $z = 2$, both *HST* imaging and adaptive optics (AO)-assisted integral field spectroscopy (IFS) at 8–10 m class telescopes barely resolve the largest clumps. Beam smearing of the velocity field can compromise
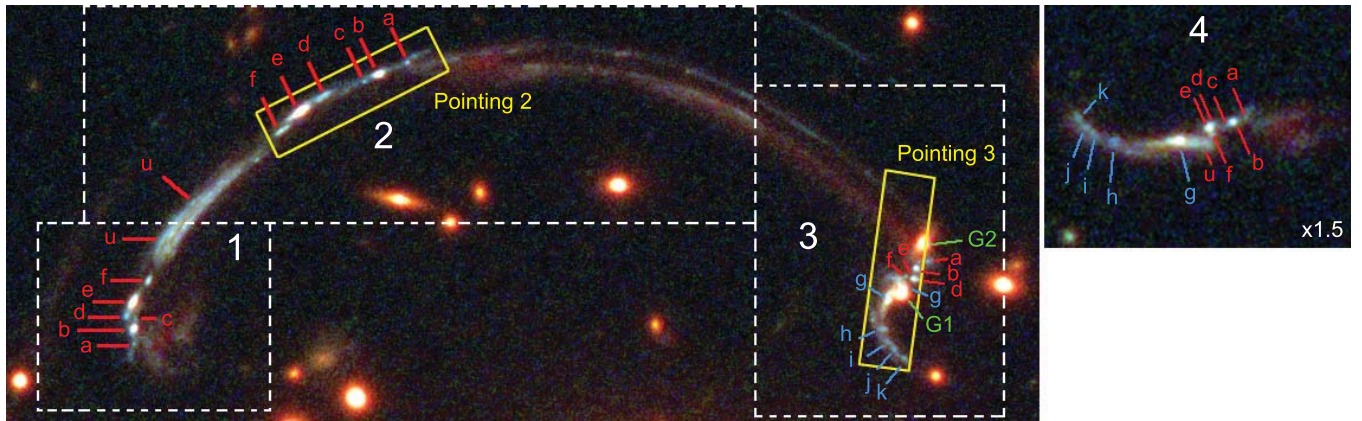
Figure 1. Identification of substructure in the giant arc and counter image of RCSGA0327 from *HST*/WFC3 imaging; north is up and east is to the left. The color rendition is composed of F160W+F125W+F098M (red), F814W+F606W (green), and F390W (blue), to highlight color gradients in the arc. The left panel extends over 35″ × 15″. The dashed lines approximately enclose the parts of the arc that compose each of the three merged images, indicated by numbers 1–3; image 4 corresponds to the counter image, which is a relatively undistorted image of the source-plane galaxy. Individual star-forming regions are labeled with letters *a*–*k*; the two cluster galaxies that fall on top of image 3 are labeled *G1* and *G2* in green. Due to the location of the source galaxy with respect to the lensing caustic, the western side (clumps *a*–*f*; red labels) appears in all of the four images, while the brightest knot of the source (labeled *g*) and the eastern "arm" (clumps *h*–*k*; blue labels) only appear in images 3 and 4. In image 3, the lensing perturbation by cluster galaxy *G1* results in another instance of clump *g*. The two OSIRIS pointings with a 1″.6 × 6″.4 field of view (FOV) and position angles (PAs) of 297° and 352° east of north are overlaid in yellow. Figure adapted from Sharon et al. (2012).

(A color version of this figure is available in the online journal.)

the kinematic classification of merger signatures as well as the analysis of turbulence, shocks, and outflows from the velocity dispersion map (e.g., Kronberger et al. 2007; Davies 2011).

Strong gravitational lensing of high-redshift background galaxies by foreground galaxy clusters can increase their apparent size by an order of magnitude or more. IFS studies of lensed galaxies have already provided detailed views of galaxy kinematics up to $z = 4.9$ (Nesvadba et al. 2006; Swinbank et al. 2009; Jones et al. 2010, 2013; Yuan et al. 2011, 2012; Shirazi et al. 2013), confirming the common occurrence of rotating disks at high redshift. The improved spatial resolution has allowed these studies to specifically address shocks and outflows (Yuan et al. 2012), metallicity gradients (Yuan et al. 2011; Jones et al. 2013), and the properties of star-forming clumps (Swinbank et al. 2009; Jones et al. 2010). In this paper, we present a detailed analysis of *HST*/Wide Field Camera 3 (WFC3) optical/near-infrared (NIR) imaging and AO-assisted Keck/OSIRIS IFS data for the brightest distant lensed galaxy currently known in the universe, RCSGA 032727-132609 at $z = 1.7$ (Wuyts et al. 2010). This combined data set probes the galaxy kinematics as well as the morphology of both the ongoing star formation and the established stellar population at spatial resolutions down to ∼100 pc in the galaxy's source plane.

This paper is organized as follows. Section 2 describes the main Keck/OSIRIS IFS observations and data reduction as well as supporting data sets from *HST*/WFC3, Keck/NIRSPEC, and Magellan/FIRE. The kinematic analysis of the IFS data is presented in Section 3 and Section 4 reports on the physical properties of the individual star-forming clumps that can be identified in both data sets. The radial variations of these properties across the galaxy are studied in Section 4.6 and the clumps are compared to scaling relations of local H II regions in Section 4.7. We present spatially resolved spectral energy distribution (SED) modeling of the system in Section 5. Section 6 summarizes the observational results and discusses what we can infer for the physics governing the morphology and kinematics of the system. Throughout this work, we adopt a flat cosmology with $\Omega_M = 0.3$ and $H_0 = 70$ km s^{-1} Mpc^{-1}. All magnitudes are quoted in the AB system.

2. OBSERVATIONS AND DATA REDUCTION

RCSGA 032727-132609, hereafter RCSGA0327, at $z = 1.703$ is the brightest and most obvious strong lensing system found in the Second Red-Sequence Cluster Survey (Gilbank et al. 2011). Its discovery, preliminary lensing analysis, and global galaxy properties are presented in Wuyts et al. (2010, 2012a). The system consists of a counter image and a giant arc that extends over 38″ on the sky and is made up of three merged images of the background source. Its intrinsic stellar mass of $6.3 \pm 0.7 \times 10^9\, M_\odot$ and SFR of 30–50 $M_\odot$ yr^{-1} (Wuyts et al. 2012a) translate into a specific SFR log(sSFR/yr^{-1}) = −8.3, which lies a factor of 3 above the main sequence of star formation at $z \sim 2$ (Daddi et al. 2007). This paper focuses on the joint analysis of *HST*/WFC3 imaging and Keck/OSIRIS IFS observations of the arc. To support the analysis, we fold in additional long-slit NIR spectroscopy from the NIRSPEC instrument on Keck and the Folded-Port Infrared Echellette (FIRE) instrument on Magellan.

2.1. HST/WFC3 Imaging

RCSGA0327 was imaged with WFC3 on *HST* under GO program 12267 (PI: Rigby). In four orbits, the source was observed with one narrowband filter targeting Hβ (F132N) and six broadband filters (F390W–F606W–F814W in the UVIS channel; F098M–F125W–F160W in the infrared channel). The imaging strategy consisted of four sub-pixel dither positions in each filter to reconstruct the point spread function (PSF), reject cosmic rays, and compensate for the chip gap. Individual frames were processed with the standard WFC3 calibration pipeline and combined using the Multidrizzle routine (Koekemoer et al. 2002). Based on the *HST* data, Sharon et al. (2012) have matched the substructure in the four different images of the source galaxy to create a robust and well-constrained lens model with magnification uncertainties ⩽10%. We adopt the naming convention introduced there and shown in Figure 1 to identify the star-forming clumps. Source-plane reconstructions of the galaxy are created by ray tracing the image pixels through deflection maps generated from the lens model.

2.2. Keck/OSIRIS Observations

We observed RCSGA0327 with the OH-Suppressing Infrared Imaging Spectrograph (OSIRIS; Larkin et al. 2006) on the Keck II telescope on two half nights of 2011 October 17–18 UT. Conditions were good with seeing measured at $0\rlap{.}''7$–$1\rlap{.}''2$. OSIRIS is an integral field spectrograph with a lenslet array to provide simultaneous NIR spectra at spectral resolution $R \sim 3600$ for up to 3000 pixels in a rectangular FOV up to $4\rlap{.}''8 \times 6\rlap{.}''4$. Due to a technical difficulty with OSIRIS at the time of observations, only the broadband filters were available. We targeted the Hα emission line with the Hbb filter in the $0\rlap{.}''1$ pixel^{-1} scale, which limits the FOV to $1\rlap{.}''6 \times 6\rlap{.}''4$. To correct for atmospheric distortion, the laser guide star AO system (LGSAO; Wizinowich et al. 2006; van Dam et al. 2006) was applied with a tip-tilt star of $R = 17.0$ at a distance of $\sim 40''$ from the giant arc. This delivers a Strehl ratio of ~ 0.2. Unfortunately, no suitable tip-tilt star was available for LGSAO observations of the counter image. Due to the limited FOV of the spectrograph and the large size of the giant arc, we were not able to observe its full extent. Figure 1 shows the two pointings we selected in the image plane; we will refer to them as pointing 2 and 3 since they target parts of the arc that correspond to images 2 and 3 of the source galaxy. Pointing 2 at a PA of $297°$ east of north corresponds to one of the most highly magnified regions of the giant arc (Sharon et al. 2012), where we can take maximal advantage of the increased brightness and spatial resolution to study clumps a through f. Pointing 3 at a PA of $352°$ east of north was chosen because it covers the full extent of the source. The early-type cluster galaxies $G1$ and $G2$ that fall on top of the arc in this pointing are not expected to show any emission lines, so they should not contaminate the Hα flux.

The observations started with short 30 s exposures of the tip-tilt star to center the pointing. These exposures are also used to calculate the PSF: two-dimensional (2D) Gaussian fits to the tip-tilt exposures yield a FWHM resolution of $\sim 0\rlap{.}''15$. From the tip-tilt star, we applied a blind offset to acquire each of the two pointings. Individual science exposures have an integration time of 900 s and are dithered by up to $0\rlap{.}''5$ around the base position to remove bad pixels and cosmic rays. Off-source sky frames were necessary because the source fills most of the narrow $1\rlap{.}''6 \times 6\rlap{.}''4$ FOV. We achieved a total on-source integration time of 1.5 hr for pointing 2 and 3.5 hr for pointing 3.

Data reduction was carried out with the OSIRIS data reduction pipeline (version 2.3),[6] which removes crosstalk, detector glitches, and cosmic rays and performs a scaled sky subtraction based on Davies (2007). Individual data cubes are mosaicked using a 3σ clipping average and the final data cube is flux calibrated based on the 2MASS H-band magnitude of the tip-tilt star. Law et al. (2009) estimate a 30% systematic uncertainty in the fluxing, largely from rapid variations of the AO-corrected PSF.

2.3. Magellan/FIRE Observations

We observed RCSGA0327 with the FIRE (Simcoe et al. 2013) at the Magellan Baade telescope in Chile on 2010 October 14–15 UT. The echelle mode delivers a continuous spectrum from 0.82–2.5 μm at a spectral resolution $R = 3600$ for the widest $1'' \times 6''$ slit. The seeing was monitored at the telescope and ranged from $0\rlap{.}''8$ to $1\rlap{.}''2$ on both nights. Based only on
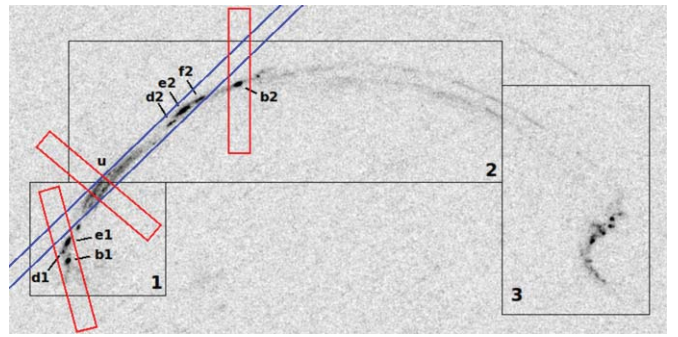
Figure 2. $32'' \times 16''$ *HST*/WFC3 image of RCSGA0327 in the F390W band. The black boxes approximately enclose each of the three images of the source galaxy that together make up the giant arc (as in Figure 1). The $0\rlap{.}''76 \times 42''$ NIRSPEC slit is shown in blue at PA = $134°$ east of north. Three pointings of the $1'' \times 6''$ FIRE slit are shown in red, targeting clumps $d1$-$e1$-$b1$ in image 1, clump u, and clump $b2$ in image 2, respectively. For simplicity, the slits are shown centered on the arc; in reality, we placed the source on the left and right sides of the slit for an ABBA nod pattern.

(A color version of this figure is available in the online journal.)

ground-based imaging, we chose three separate positions of the arc, as shown in Figure 2. With the *HST* imaging, we now know that they correspond to clumps $b1$-$d1$-$e1$ in image 1, clump u, and clump $b2$ in image 2. The pointings were acquired through a blind offset from a nearby cluster galaxy; source acquisition was verified with the NIR slit-viewing camera. The observations consisted of four individual 600 s exposures for each pointing, nodded along the slit in an ABBA pattern. The telluric star HD 21875 was observed every hour for flux calibration purposes. We reduced the data using the custom pipeline provided by R. Simcoe (Simcoe et al. 2013), which uses OH skylines for wavelength calibration and performs sky subtraction using the techniques presented by Kelson (2003). The extracted spectra for clumps u and $b2$ are shown in Figure 4. We cannot spatially resolve clumps $b1$, $d1$, and $e1$ covered by the pointing in image 1. Since clumps $b1$ and $e1$ are of comparable brightness, we cannot derive line fluxes for individual clumps from this pointing and do not consider it further.

For each spectrum, we simultaneously fit all emission lines with a multi-component Gaussian model, using the IDL Levenberg–Marquardt least-squares fitting code MPFITFUN (Markwardt 2009). We obtain an initial fit of the bright Hα emission line to establish a first guess for the redshift and linewidth. For the combined fit, we set the initial wavelength centroids of all lines based on their NIST rest wavelengths[7] and allow them to vary by up to three times the 1σ uncertainty from the initial fit to allow for errors in the wavelength calibration. For each spectrum, all lines are forced to share a common velocity width, since the nebular emission is expected to originate from the same physical region within the galaxy. We report the flux measurements in Table 1. In the FIRE spectrum of clump u, the [Ne III] λ3869 emission line is not detected. We derive an upper limit as the flux contained within a Gaussian with the common linewidth and a peak value equal to twice the noise at the expected line center.

2.4. Keck/NIRSPEC Observations

We obtained a total of 1.3 hr of NIR long-slit spectroscopy of RCSGA0327 with Keck/NIRSPEC on 2010 February 4 UT, targeting the brightest $10''$ of the arc at a PA of $134°$ east of north

---

Table 1
Measured Line Fluxes from NIRSPEC and FIRE

Emission Line	NIRSPEC		FIRE	
	Clump u	Clump $e2$	Clump u	Clump $b2$
[O II] λ3727	544 ± 13	189 ± 8	12.6 ± 1.1	2.3 ± 0.2
[Ne III] λ3869	64 ± 5	30 ± 3	<1.8	0.69 ± 0.05
Hγ	68 ± 3	50 ± 2	2.4 ± 0.3	0.64 ± 0.04
Hβ	171 ± 3	119 ± 2	5.8 ± 0.3	1.40 ± 0.04
[O III] λ4959	275 ± 2	189 ± 2	10.1 ± 0.5	2.99 ± 0.07
[O III] λ5007	909 ± 4	611 ± 3	44 ± 1	7.28 ± 0.12
Hα	675 ± 3	388 ± 2	26.1 ± 0.5	4.82 ± 0.06
[N II] λ6583	34 ± 4	51 ± 3	1.3 ± 0.2	0.20 ± 0.02

Notes. Fluxes are in units of 10^{-17} erg s^{-1} cm^{-2}.

(Figure 2) with three grating settings (NIRSPEC filters N1, N3, and N6). Detailed analysis of the collapsed one-dimensional (1D) spectra was published in Rigby et al. (2011, hereafter R11). The subsequently obtained *HST*/WFC3 imaging revealed that the slit position covered several individual star-forming regions: clumps $f2$, $e2$, and $d2$ in image 2 and clump u shared between image 1 and 2. Here, we re-analyze the spectra to quantify the spatial variation of line fluxes and line ratios across the clumps.

Details of the observations and the data reduction can be found in R11. Figure 3 shows the 2D spectra for the main emission lines. The spectra are dominated by emission from clumps u and $e2$, which are clearly resolved. Clump $e2$ has a ~20% contribution from clumps $f2$ and $d2$, which cannot be separated. To compensate for differential seeing and slit losses, we apply the same bulk scaling of the N1 and N6 filters relative to the N3 filter as in R11. We again note that the relative fluxing should be excellent within a single grating setting, but from one grating setting to another the relative flux offsets may be large. The extracted 1D spectra of clumps u and $e2$ are plotted in Figure 4.

For each clump and grating setting, we simultaneously fit all emission lines as described above for the FIRE spectra; line fluxes can be found in Table 1. Adding line fluxes for clumps u and $e2$ generally agrees within 2σ of the line fluxes published in R11. The absolute flux values of clump u should not be compared between the FIRE and NIRSPEC spectra, since we have not applied any aperture correction between both slits. We can address the relative fluxing of the different gratings by comparing line ratios for clump u with the ratios measured in the FIRE spectrum of this clump. Using [O II] λ3727 in N1, Hγ, Hβ, and [O III] λ4959 in N3 and Hα in N6, we find a weighted mean offset of 9%, 35%, and 40% for N6–N3, N3–N1, and N6–N1, respectively. We caution that the only bright line in N1, the [O II] λ3727 doublet, is difficult to measure accurately.

3. GALAXY KINEMATICS

3.1. Mapping the Velocity Field

We create spatial and kinematic maps of the Hα emission in RCSGA0327 by fitting a Gaussian profile to the Hα emission line for every spatial pixel. The noise is estimated separately from a blank region of sky in each of the pointings. A minimum signal-to-noise ratio (S/N) of 4.5σ is required for a detection of Hα; if this criterion is not met, the surrounding 3×3 spatial pixels are averaged and the fit is re-attempted. Formal uncertainties are derived for each spatial pixel from fitting 100 mock spectra consistent with the noise. The relative shifts of the wavelength centroid of the Hα emission line translate into a
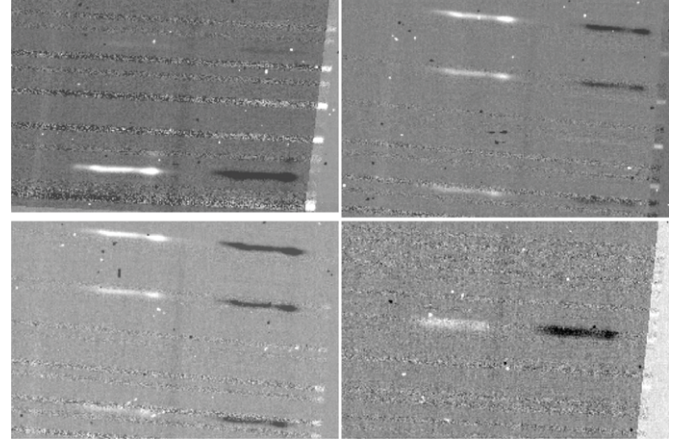
Figure 3. 2D sky-subtracted, nod-subtracted NIRSPEC spectra of RCSGA0327. Each frame is a subtraction of two nods, with one nod as light and the other as dark. In each panel, wavelength increases from bottom to top. Counterclockwise from top left, the panels show: (top left) the N6 spectrum, with Hα, the [N II] doublet, and [S II], (top right) the N3 spectrum, with Hβ and the [O III] λ4959,5007 doublet, (bottom left) same as top right, but two additional nods, and (bottom right) the N1 spectrum, with [O II] λ3727.

velocity map of the ionized gas. We define an absolute velocity zeropoint based on the Hα centroid determined for clump e from the NIRSPEC spectra (Section 2.4), which corresponds to $\lambda_{H\alpha} = 1.774903 \pm 0.000003$ μm or $z = 1.7037455 \pm 0.000005$. After applying a barycentric correction to the OSIRIS wavelength calibration, we find a wavelength shift of 1.1 Å for pointing 2 and 0.7 Å for pointing 3, well within the OSIRIS wavelength calibration uncertainty of up to 5 Å.[8] We correct the calibration of both pointings for these wavelength shifts.

The Hα flux, velocity, and velocity dispersion maps are transformed into the source plane and shown in Figures 5 and 6. The maps are smoothed with a boxcar average of 3 pixels for the purpose of visualization. The velocity dispersion is corrected for the instrument response function by subtracting the instrumental resolution in quadrature. This is determined from Gaussian fits to the OH sky lines and corresponds to a FWHM of 5.6 Å. Typical uncertainties in the velocity and velocity dispersion maps are ~10 km s^{-1}. The x- and y-axes of the maps have been centered on the brightest clump, clump g. To allow the source-plane transformations, the OSIRIS maps have to be aligned with the *HST* images on which the lens model is based. This is done visually, using the positions of the various clumps in both data sets. While this alignment does not produce global spatial accuracy to better than one OSIRIS pixel (0″.1), it does not influence the comparison of the relative location of multiple emission features within each pointing.

The velocity map agrees with the velocity offsets between clumps measured in the FIRE and NIRSPEC data. Based on the Hα emission line centroid, we find $\delta v = 15 \pm 1$ km s^{-1} between clumps u and $e2$ from the NIRSPEC spectra and $\delta v = 44 \pm 3$ km s^{-1} between clumps u and $b2$ from the FIRE spectra.

3.2. Analyzing the Velocity Field

The velocity map shown in Figure 5 is well structured and contains a strong velocity gradient. We define a kinematic axis connecting the maximum and minimum velocity regions and extract a 1D velocity profile as the median and standard

---

[8] http://irlab.astro.ucla.edu/osiriswiki/
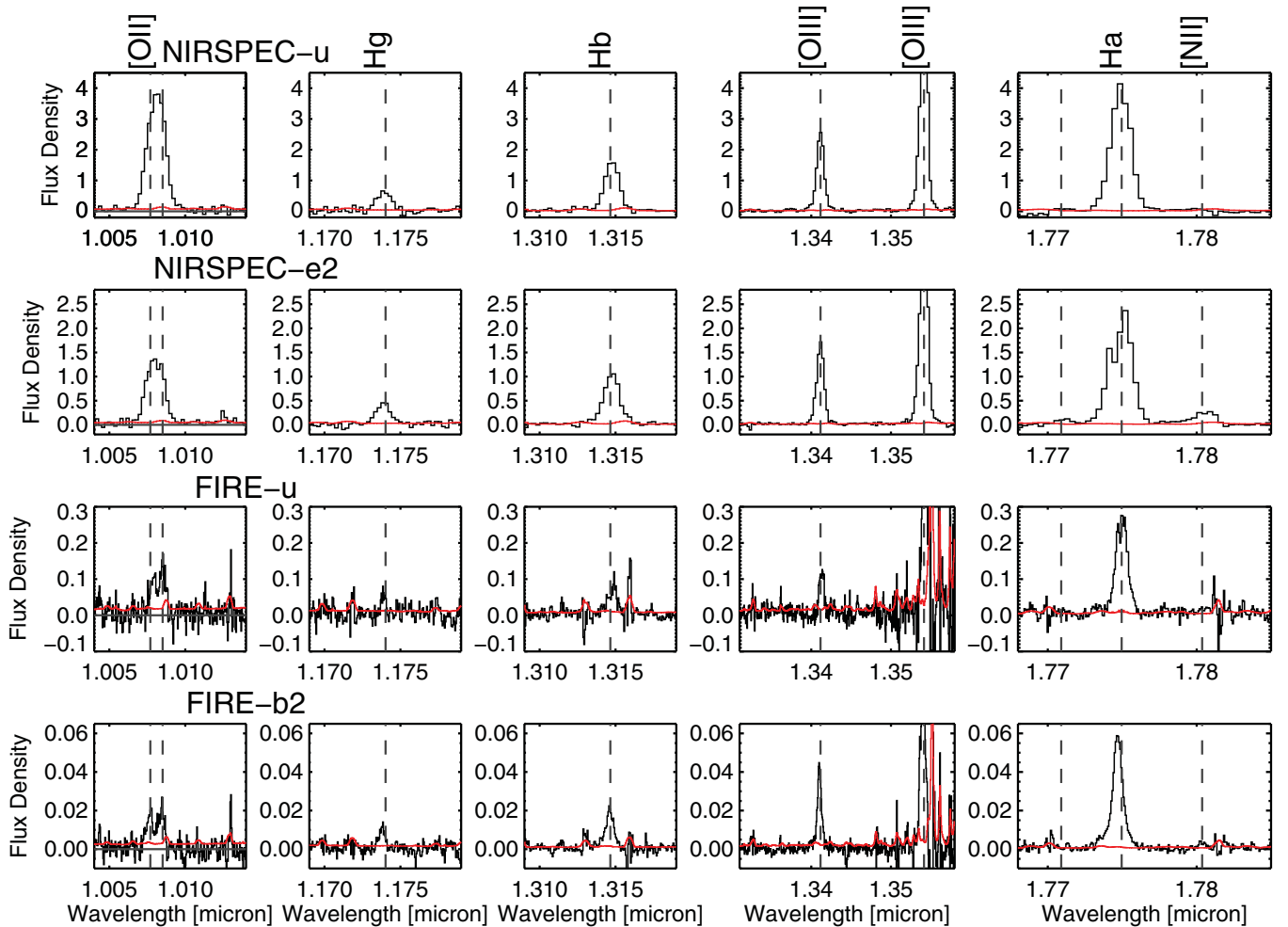
Figure 4. Extracted NIRSPEC spectra for clumps *u* and *e*2 and extracted FIRE spectra for clumps *u* and *b*2. Three wavelength ranges are chosen to show the [O II] λ3727, Hγ, Hβ, [O III] λ4959,5007, Hα, and [N II] emission lines. The 1σ error spectra are shown in red. The *y*-axis shows specific flux density in units of 10^{-16} erg s^{-1} cm^{-2} Å^{-1}.

(A color version of this figure is available in the online journal.)

deviation within bins of 0.7 kpc width along this axis (Figure 7, top panel). The bins were chosen in correspondence with the FWHM of the OSIRIS data cubes such that individual data points in the 1D profile represent independent measurements. The locations of clumps *g*, *e*, and *b* are shown for reference. This 1D profile does not display the smooth S-shaped curve expected from a rotating disk but instead levels off to a plateau between clumps *g* and *e*. This suggests the system is currently undergoing an interaction. The bottom panel in Figure 7 shows the 1D velocity profile extracted along the solid line in Figure 5 (PA = 40° east of north). This corresponds to a region of clumpy emission (clumps *h–k*; see Figure 1) that extends from clump *g* toward the northeast and shows blue broadband rest-frame UV colors. The velocity profile agrees with the expectation for a tidal tail swinging away from the observer and curving back into the plane of the sky: the velocity peaks in the middle and falls off to either side. Within this interpretation, separate star-forming knots in the tail (clumps *h–k*) might evolve into tidal dwarf galaxies (e.g., Mihos & Bothun 1998; Hibbard et al. 1994; Duc et al. 2000).

The gray diamonds in Figure 7 (shifted down in velocity to improve the clarity of the figure) illustrate the coarser spatial resolution that would be obtained without lensing magnification. The velocity peak in the tidal tail remains visible, but the plateau between clumps *g* and *e* would be largely smoothed

out, resulting in an ambiguous velocity profile that could easily be interpreted as a single rotating disk.

The velocity dispersion maps contain additional kinematic information. For a rotating disk at higher redshift, the dispersion is typically seen to increase toward the center due to beam smearing of the velocity gradient (e.g., Epinat et al. 2010). Additionally, areas of active star formation, like clumps, can show elevated velocity dispersion because of outflows (Newman et al. 2012b). RCSGA0327 shows a noticeable peak in velocity dispersion at the location of clump *e*, which agrees with the detection of a strong outflow from this clump presented in Section 4.4. The other two peaks in velocity dispersion are located between clump *g* and the tidal tail and likely originate from increased turbulence due to the ongoing interaction. Additionally, elevated velocity dispersions could be caused by overlapping components along the line of sight, where the Hα profile consists of two emission lines separated slightly in velocity. Attempting to fit the Hα emission with a single Gaussian function will result in an overestimate of the linewidth. This has been seen in local mergers (e.g., Mihos & Bothun 1998), but we lack sufficient S/N to robustly identify any such multiple Hα emission peaks in the OSIRIS data.

The physical extent of RCSGA0327 further strengthens the kinematic arguments for an ongoing interaction. We estimate the size of the system from a segmentation map of all pixels >3σ in
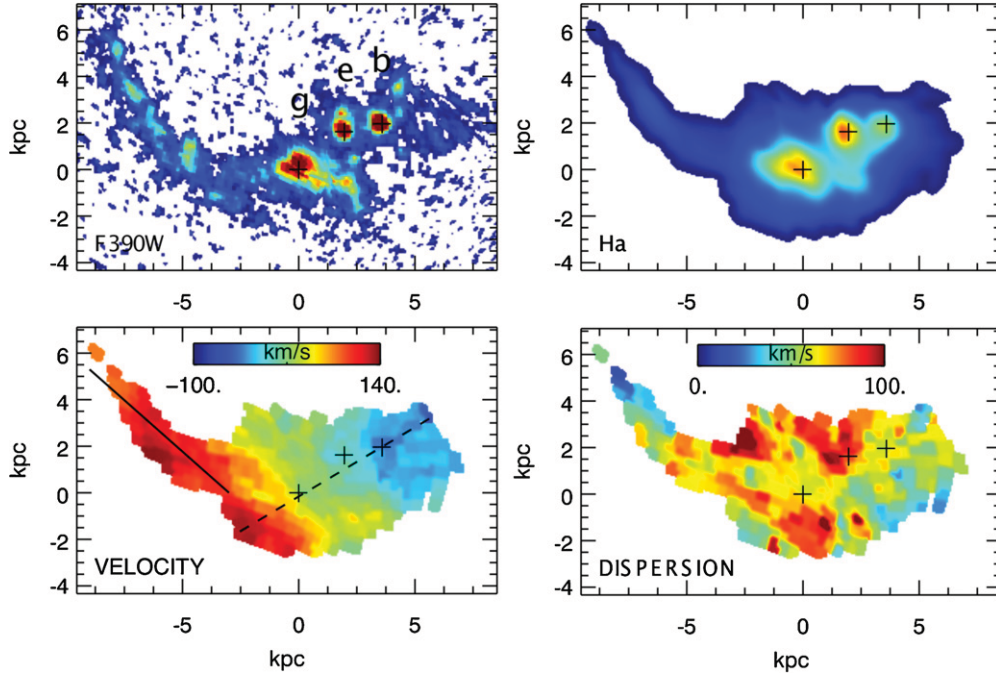
Figure 5. Source-plane maps of the F390W flux, Hα flux, velocity, and velocity dispersion for image 3. The latter three maps are smoothed with a boxcar average of 3 pixels for the purpose of visualization.The x- and y-axes are centered on clump g; clumps g, e, and b are marked by black crosses (from left to right). The kinematic axis and the axis along the "arm" that extends to the northeast from clump g are overlaid on the velocity map as dashed and solid lines, respectively.

(A color version of this figure is available in the online journal.)
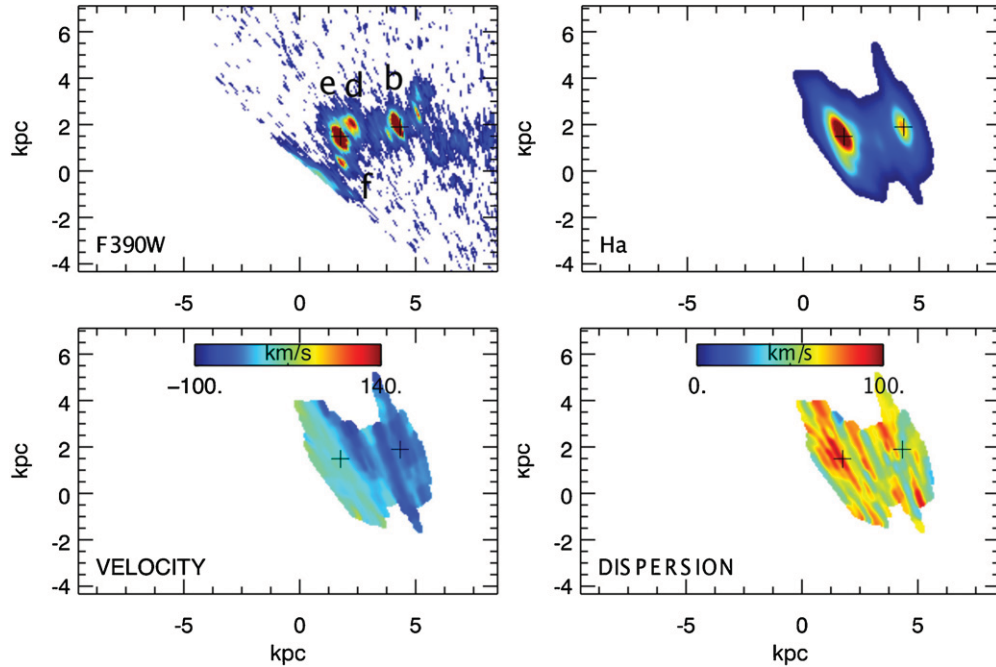
Figure 6. Source-plane maps for image 2, which contains a smaller, but more highly magnified part of the source-plane galaxy. The size, centering, and scaling of the maps is identical to Figure 5. Clumps e and b are marked by black crosses (from left to right).

(A color version of this figure is available in the online journal.)

the source-plane F160W image, including the arm that extends to the northeast. With a radius $r_e = \sqrt{A/\pi} = 7.1$ kpc and a stellar mass of $6 \times 10^9 \, M_\odot$ (Wuyts et al. 2012a), RCSGA0327 lies near the upper extreme of the size-mass relation of SFGs at $z \sim 2$, even when taking into account the considerable scatter in this relation (Franx et al. 2008; Williams et al. 2010; Wuyts et al. 2011; Barro et al. 2013). Thus, as an isolated

galaxy, this system would be unusually large for its stellar mass.

4. PHYSICAL PROPERTIES OF CLUMPS

This section covers measurements of the individual star-forming regions that can be identified in RCSGA0327. From the WFC3 imaging, we measure broadband photometry and use
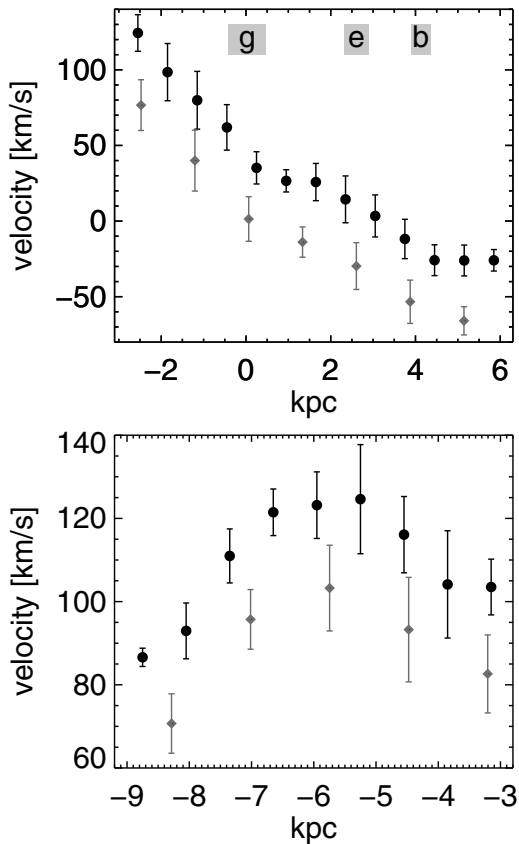
Figure 7. Top: 1D velocity profile of the source-plane galaxy along its kinematic axis, constructed from the median and standard deviation of the velocity map in 0.7 kpc wide bins. The locations of clumps *g*, *e*, and *b* are indicated for reference. Bottom: 1D velocity profile along the "arm" extending toward the northeast from clump *g*, indicated by the solid line in Figure 5. The peak in velocity near the middle of the arm is typical for a tidal tail. In both panels, the gray diamonds indicate the coarser spatial resolution available without lensing magnification; the points are shifted down in velocity by 40 km s^{-1} and 20 km s^{-1} in the top and bottom panels, respectively, to improve the clarity of the figure.

SED modeling to constrain the stellar populations of the clumps: age, stellar mass, extinction, and SFR. Integrated Hα spectra are created for each clump from the OSIRIS data, from which velocity dispersion, SFR, metallicity, and outflow properties can be derived.

4.1. Broadband Photometry

The photometric analysis of the clumps is performed in the image plane because the PSF is not well defined in the source-plane reconstructions. It varies across the source plane depending on the location with respect to the lensing caustic and has an elliptical shape due to the non-isotropic magnification (see Sharon et al. 2012 for more details). The clumps are identified in the higher resolution WFC3/UVIS images; we transform the WFC3/IR images to the same reference for a uniform photometry measurement. A series of elliptical apertures of increasing radial extent are defined for each region. The ellipticity changes according to how significantly the clumps are stretched by the lensing. We measure the flux at a radius of roughly twice the FWHM and use the zeropoint and aperture corrections (typically 15%–25%) as defined in the WFC3 handbook.[9]

The clumps are embedded in the galaxy and the removal of underlying galaxy background light has to be handled carefully. At rest-frame UV wavelengths, the contribution of the diffuse galaxy background is often ignored since the clumps are typically two to four times as bright as their surroundings (Elmegreen et al. 2009). However, the lensing magnification of RCSGA0327 allows us to study smaller and fainter clumps; we find that the galaxy background accounts for 30%–80% of the total flux in the clump apertures. Additionally, the contrast between the clumps and the background is lower at rest-frame optical wavelengths, where the emission of bright, young stars is less dominant. Following Guo et al. (2012), we determine the background for each WFC3 band as all pixels that belong to the galaxy (i.e., that lie above a threshold of 3σ) and do not fall within one of the photometric clump apertures. The *global* background is then simply the average value of these background pixels. We also define a *local* background for each clump as the mean and standard deviation of the background pixels within an annulus of width $\sim$0$.\!\!''$4 outside the clump aperture. For RCSGA0327, the local backgrounds generally agree with the global estimate. Similarly, Guo et al. (2012) find that the change in rest-frame UV colors between a global and local background subtraction for $z \sim 2$ SFGs in the Hubble Ultra Deep Field is not statistically significant. However, it remains important to check this consistently in future studies since an incorrect assumption of a constant global background across the galaxy can introduce false radial variations in clump color and related properties.

Outliers within the clump apertures, such as contributions from neighboring clumps, are masked by hand. Identifying exactly which pixels should be masked can be uncertain in the IR images where the larger PSF blends close overlapping neighbors such as clumps *d*, *e*, and *f* in image 2 and clumps *d*, *e*, and *b* in image 3. In those cases, the added flux uncertainty is typically 10%. In image 3, the two cluster galaxies that fall on top of the arc are removed before measuring the clump photometry, using the technique presented in Wuyts et al. (2010). In short, for each WFC3 band we subtract a scaled F390W image to remove the arc. Any remaining positive flux at the positions of the cluster galaxies is then subtracted and the original frame is restored by adding the scaled F390W image back in. Final magnitudes are corrected for Galactic extinction (Schlegel et al. 1998). The photometric uncertainties include Poisson noise, an absolute WFC3 zeropoint uncertainty of 1%, an uncertainty in the background subtraction determined from the standard deviation of the local background value, and an uncertainty from the masking of neighboring clumps. The background subtraction dominates the total uncertainty.

For the galaxy-integrated photometry measurement of RCSGA0327, the contribution of rest-frame optical nebular emission lines to the NIR photometry was estimated at 5%–10%, which is negligible compared with the photometric uncertainties (Wuyts et al. 2012a). However, individual star-forming regions have much higher star formation surface densities than the host galaxy as a whole, such that the nebular emission adds a sizeable, and possibly dominant, contribution to the NIR light. At the redshift of RCSGA0327, the F098M band includes the [O II] λ3727 emission line, while Hβ and the [O III] λ4959,5007 doublet are the most important contaminating lines for the F125W band. Hα falls just redward of the F160W band. The removal of this nebular line emission from the broadband photometry is not trivial. We can use the F132N narrowband image to measure the Hβ line emission within each of the clump apertures
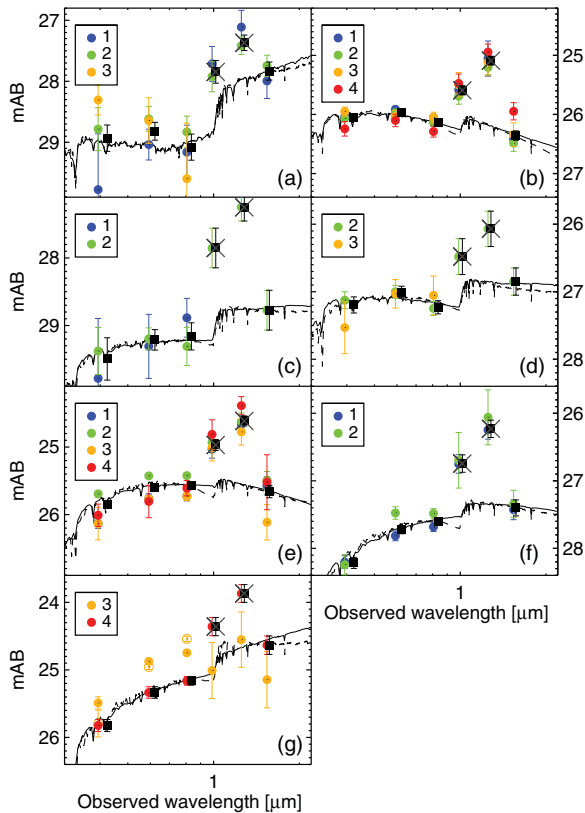
Figure 8. Final photometry for the clumps as measured from the six WFC3 UVIS and IR bands, corrected for the lensing magnification. The measurements from the multiple images of the source are in reasonable agreement. The black squares correspond to the weighted mean and uncertainty in the mean of the photometry for each clump; they are shifted slightly in wavelength to improve the clarity of the figure. The F098M and F125W magnitudes are not corrected for nebular line emission; they are shown with large gray crosses in all panels and are not included in the SED fit. The best-fit SED to the weighted mean UVIS+F160W photometry is shown in black, with a solid line for the default Calzetti extinction law and a dashed line for the SMC extinction law.

(A color version of this figure is available in the online journal.)

used for the broadband photometry. Knowledge of the line ratios of Hβ to the [O II] and [O III] emission lines then allows removal of the line contamination from the F098M and F125W fluxes. However, the NIRSPEC and FIRE data show that these line ratios can vary across the arc by more than a factor of two (Table 1). Correcting individual clumps for emission-line contamination therefore adds large uncertainties to the F098M and F125W photometric uncertainty, which results in minimal constraints on the observed spectral energy distribution. For this work, the F098M and F125W bands remain uncorrected and are not included in the SED modeling described below.

Finally, the photometry for each clump needs to be corrected for the lensing magnification. Using the magnification map presented in Sharon et al. (2012), we derive individual clump magnifications as the flux-weighted mean magnification within the photometric clump aperture. Figure 8 shows the demagnified AB magnitudes for each of the clumps in the multiple images of the source galaxy. Not all clumps are present in all images and some of the clumps are too faint and/or blended for an accurate measurement, especially in the WFC3/IR bands. There is a general agreement between the independent clump measurements from the multiple images, which confirms the robustness of the photometry method. The weighted mean and uncertainty in the mean derived from the available measurements for each clump

are shown with black data points. We use this weighted mean in all subsequent analysis. Image 3 is complicated by the presence of cluster member G1 (see Figure 1), which appears to split clump g in two images. The photometry of those two images (shown with open and filled orange circles in the bottom left panel of Figure 8) does not agree with the well-measured appearance of clump g in image 4. Given this lensing complexity, we discard the measurements of clump g from image 3.

4.2. SED Modeling

The stellar populations of the clumps can be constrained with SED modeling of the observed clump photometry. We use the SED fitting code FAST (Kriek et al. 2009) at a fixed spectroscopic redshift with the Bruzual & Charlot (2003) stellar population synthesis models (BC03), a Chabrier (2003) initial mass function (IMF), and a Calzetti et al. (2000) dust extinction law. The metallicity is restricted to 0.2 or 0.4 $Z_\odot$ for all clumps, consistent with the oxygen abundance measured from the integrated NIRSPEC spectrum (R11), as well as the metallicity measurements of individual clumps from the OSIRIS, FIRE, and NIRSPEC data (see Section 4.4). We initially adopt exponentially decreasing star formation histories (SFHs) with a minimum e-folding time $\log(\tau) = 8.5$ and a minimum age limit of 50 Myr. Wuyts et al. (2011) shows good agreement between SFR estimates based on these assumptions and other multi-wavelength SFR indicators out to $z \sim 3$. This default fit returns best-fit models at the age cut-off of 50 Myr for all clumps except clump a. Removing the age limit significantly improves the fit and returns ages between 3 and 16 Myr, albeit with large uncertainties. The 50 Myr age limit roughly corresponds to the dynamical timescale of a $z \sim 2$ galaxy and is typically included to avoid a luminosity bias from the most recently formed O and B stars in the SED fit. However, star-forming clumps have much shorter dynamical timescales ($t_{\rm dyn} \sim r/v \sim 5$ Myr) and in the local universe star clusters are often dated between a few and a few tens of Myr (e.g., Bastian et al. 2006). We caution that these age estimates should be interpreted as the age of the current episode of star formation within the regions, which outshines the contribution of a possible underlying older stellar population (age >100 Myr).

The best-fit SED models for the weighted mean photometry of each clump are shown in Figure 8 and 68% confidence intervals for the stellar population parameters are reported in Table 2. The stellar masses fall below the typical clump masses of 10^8–10^{10} $M_\odot$ reported in non-lensed studies (Förster Schreiber et al. 2011; Guo et al. 2012) and lie closer to the range of 10^6–10^8 $M_\odot$ found for a lensed spiral galaxy at $z = 1.5$ (Adamo et al. 2013). As is often seen in SED modeling, the e-folding time τ is not constrained by the fit.

The SFRs derived from the best-fit models are very high, especially for clumps e and g with 110 and 60 $M_\odot$ yr^{-1}, respectively. From a range of different SFR indicators, Wuyts et al. (2012a) estimate a galaxy-integrated SFR for RCSGA0327 of 30–50$M_\odot$ yr^{-1}. This suggests that the SED fit is overestimating the SFR of individual clumps. We experimented with alternative SFHs by including (1) exponentially declining models with shorter e-folding times τ down to 10 Myr, (2) delayed histories with SFR $\sim t \exp(-t/\tau)$, and (3) inverted models with SFR $\sim \exp(t/\tau)$. The stellar population parameters remain within the 1σ uncertainties of the default fit for all these alternative SFH templates. At the young clump ages of $\lesssim$20 Myr, the shape of the SFH has a negligible impact on the best-fit

Table 2
Clump Stellar Population Parameters and Radii

	Calzetti Extinction				SMC Extinction			r_{cl}
	Age (Myr)	$E(B-V)_s$	$\log(M_*/M_\odot)$	SFR ($M_\odot$ yr^{-1})	Age (Myr)	$E(B-V)_s$	SFR ($M_\odot$ yr^{-1})	(pc)
a	3200^{+0}_{-2800}	$0.02^{+0.13}_{-0.02}$	$8.1^{+0.1}_{-0.5}$	$0.05^{+0.10}_{-0.02}$	2500^{+1250}_{-1350}	$0.00^{+0.04}_{-0.00}$	$0.05^{+0.02}_{-0.01}$	250 ± 120
b	6^{+21}_{-5}	$0.17^{+0.10}_{-0.10}$	$7.7^{+0.5}_{-0.2}$	8^{+124}_{-6}	8^{+1}_{-2}	$0.07^{+0.01}_{-0.01}$	$3.3^{+0.9}_{-1.0}$	180 ± 100
c	10^{+1140}_{-9}	$0.25^{+0.2}_{-0.25}$	$6.8^{+0.8}_{-0.2}$	1^{+24}_{-1}	90^{+420}_{-70}	$0.07^{+0.04}_{-0.07}$	$0.05^{+0.09}_{-0.04}$	270 ± 160
d	16^{+573}_{-13}	$0.17^{+0.14}_{-0.17}$	$7.5^{+0.6}_{-0.2}$	2^{+12}_{-2}	100^{+220}_{-90}	$0.04^{+0.04}_{-0.00}$	$0.4^{+0.3}_{-0.2}$	320 ± 190
e	3^{+1}_{-2}	$0.32^{+0.03}_{-0.08}$	$8.5^{+0.1}_{-0.4}$	110^{+220}_{-90}	11^{+9}_{-5}	$0.11^{+0.04}_{-0.00}$	$5.0^{+8.3}_{-1.0}$	170 ± 120
f	5^{+2}_{-4}	$0.37^{+0.08}_{-0.06}$	$7.7^{+0.4}_{-0.2}$	9^{+91}_{-4}	22^{+18}_{-14}	$0.15^{+0.00}_{-0.04}$	$0.6^{+0.4}_{-0.4}$	160 ± 80
g	8^{+65}_{-7}	$0.37^{+0.13}_{-0.12}$	$8.7^{+0.5}_{-0.1}$	60^{+1320}_{-50}	64^{+116}_{-28}	$0.11^{+0.04}_{-0.00}$	$3.1^{+2.1}_{-2.4}$	200 ± 140

stellar population parameters and is therefore not causing the high clump SFRs.

The SED-derived SFR estimates can be reduced by assuming a different dust extinction law. It has been suggested that the assumption of a patchy dust distribution inherent in the Calzetti dust extinction law might not be a good representation of the dust geometry in young SFGs at $z \sim 2$ and could significantly overpredict their dust extinction (Reddy et al. 2006; Siana et al. 2009; Wuyts et al. 2012a). The large covering fraction of outflowing gas observed for two $z \sim 2$ lensed SFGs inferred from the presence of opaque interstellar absorption lines in their rest-frame UV spectra (Siana et al. 2008, 2009) is indicative of a more uniform foreground sheet of dust. This results in a steeper extinction law, such as the one derived for the Small Magellanic Cloud (SMC; Prevot et al. 1984). Rest-frame UV spectra of clumps $e2$ and u in RCSGA0327 taken with the MAGE spectrograph at Magellan show similar opaque absorption lines (J. R. Rigby et al. 2014, in preparation). When adopting the SMC extinction law in the SED fit, we cannot distinguish the best-fit models from the Calzetti result in terms of χ^2 statistics. The best-fit models and derived stellar population parameters are included in Figure 8 and Table 2. The SFRs of clumps e and g are now 5 and 3.1 $M_\odot$ yr^{-1}, respectively, a more plausible result in light of both the galaxy-integrated SFR and the Hα-derived clump SFRs (see Section 4.4). The reddening is lower due to the steeper extinction curve and the stellar ages are overall higher than for the Calzetti fit. The stellar mass is consistent within the 1σ uncertainties and therefore not included in Table 2.

4.3. Clump Size

Accurately determining the sizes of the individual clumps is not trivial. In the literature, region size is often measured from the area above a chosen surface brightness level. This isophote method has a few important problems. First of all, the surface brightness threshold is typically determined visually, from a trade-off between identifying a maximum number of regions while minimizing blending between individual regions. The chosen isophote is thus subjective and difficult to compare between studies, especially over a range of redshifts. Second, this method can be influenced significantly by local background variations, especially at high redshifts where undetected low surface brightness regions or overlap light from regions that are only separated by a few pixels can enhance the local background level. Finally, and most importantly, the isophote method will automatically find brighter regions to be larger, since more of the diffuse outskirts of the region will fall above the chosen isophote.

A more robust way to measure region size is provided by the core method, in which a 2D light profile is fit to the surface brightness profile of each region (e.g., Wisnioski et al. 2012). The local background is a free parameter in the profile fit, thus minimizing its influence on the size measurement. Most commonly, a 2D Gaussian light profile is used, which probes primarily the central ionized core of the H II regions. Adopting this method, we use GALFIT (version 3.0; Peng et al. 2010) to create a model for each individual star-forming region in the F390W image, using a Tiny Tim model for the PSF (Krist et al. 2011). The F390W image is chosen for the profile fit because the contrast between the clumps and the background is largest in this bluest *HST* band. A single Gaussian profile provides an adequate fit for most regions, except for the brightest ones, clumps b, e, and g. There, an additional Gaussian component is required to model the surrounding diffuse nebula, which is bright enough to rise above the background level. The best-fit GALFIT models are deconvolved and mapped back to the source plane. We define the clump radius r_{cl} as the effective 1σ Gaussian width of the source-plane model. Table 2 reports the weighted mean of the radii measured for the multiple images of each clump. The uncertainties of 50%–70% reflect the scatter in size measurements for the same clump in the multiple images of the source, a systematic uncertainty of 30% to account for uncertainties introduced when the clumps are not truly Gaussian, and resolution effects (Wisnioski et al. 2012).

The clumps in RCSGA0327 range in size from $\sim$300 to 600 pc (quoted here as the clump diameter). Clumps studied in other lensed galaxies in the literature occupy a similar size range of $\sim$300–1000 pc (Swinbank et al. 2009; Jones et al. 2010; Livermore et al. 2012). This is significantly smaller than the clump sizes of 1–2 kpc typically measured for non-lensed galaxies (e.g., Genzel et al. 2011; Wisnioski et al. 2012), where the limited available resolution can blend neighboring clumps into larger, more luminous regions. Additionally, since lensing studies typically target less massive galaxies, they are expected to probe less massive, smaller clumps.

4.4. Clumps in OSIRIS

The OSIRIS data provide additional information on the individual star-forming regions. To avoid the ill-defined source-plane PSF as well as uncertainties introduced when mapping the OSIRIS data to the *HST* reference frame and subsequently to the galaxy source plane, the clumps are identified and characterized in the image-plane data cubes. Implementing the core method for region identification, we fit multiple 2D Gaussian profiles simultaneously to the Hα intensity maps. This identifies clumps
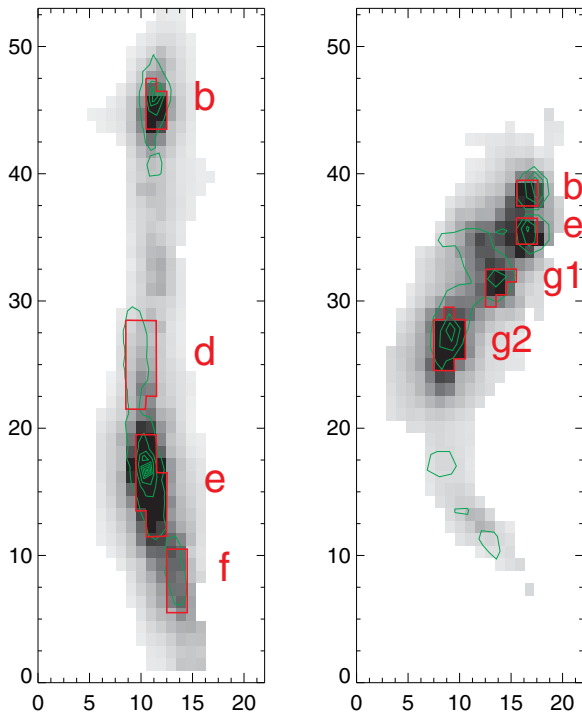
Figure 9. Image-plane Hα emission maps for pointing 2 (left) and pointing 3 (right), overlaid with F390W flux contours in green. The maps show the total Hα flux in each spatial pixel in the OSIRIS data cubes, as derived from Gaussian fits to the line profile (see Section 3.1). The clump apertures are shown in red. These result from the simultaneous fit of multiple 2D Gaussians to the Hα emission maps and correspond to the 1σ extent of the best-fit 2D Gaussians.
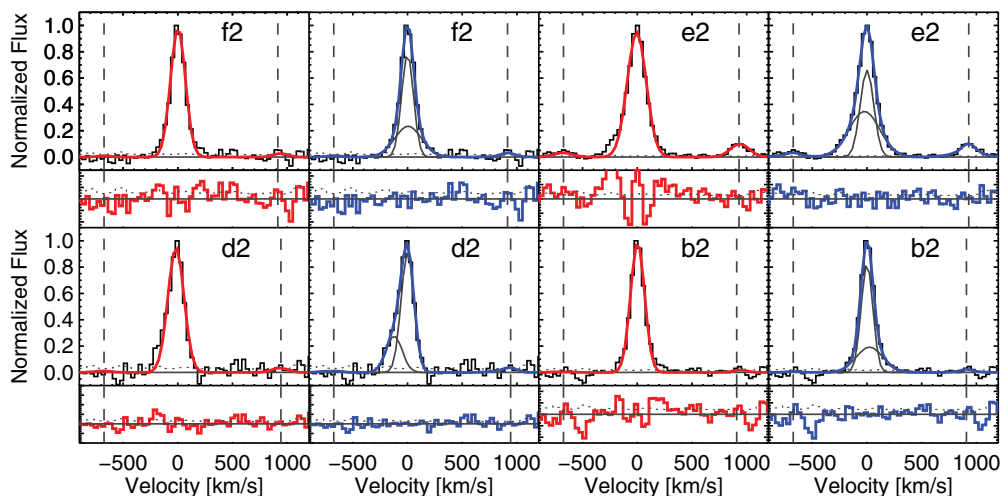
(A color version of this figure is available in the online journal.)

maps for both pointings, overlaid with the F390W contours in green. The clump apertures are marked in red. There is good agreement between the rest-frame UV and Hα morphologies.

An integrated spectrum is constructed for each clump by adding all the spatial pixels within its aperture. We note that typical rotation signatures across individual clumps are insignificant compared with the velocity uncertainties; shifting all pixels to a common central wavelength to correct for velocity broadening has a negligible influence on the shape of the integrated spectra. As discussed above, the core method provides a more robust region identification compared with the subjective isophote method. The total Hα emission will be somewhat underestimated due to diffuse emission beyond the clump aperture, which is aggravated by an imperfect Strehl ratio for the AO correction. The wavelength centroid and linewidth do not depend critically on the clump aperture.

In pointing 2, single Gaussian fits to the integrated spectra fail to fit the broad wings of the Hα emission line, as can be seen in Figure 10. The line profiles include a broad underlying component, which signifies the presence of outflows. Star-formation-driven galactic winds are seen in most high-redshift SFGs (e.g., Shapiro et al. 2009; Weiner et al. 2009; Rubin et al. 2010; Steidel et al. 2010) and have recently been localized for a handful of massive, individual star-forming clumps (Genzel et al. 2011; Newman et al. 2012b; Wisnioski et al. 2012). Following Newman et al. (2012b), we fit the Hα line profile with a double-component Gaussian model when it improves the reduced χ^2 of the fit over the Hα and [N II] region ($\sim$145 degrees of freedom) by at least 10%. This is the case for all clumps in pointing 2; none of the line profiles in pointing 3 have sufficient S/N to detect an underlying broad component. The line profile parameters are reported in Table 3. The luminosities are corrected for the flux-weighted mean magnification within the OSIRIS clump aperture and the linewidths are corrected for instrumental broadening. Clump SFRs are derived from the narrow-component Hα luminosities with the Kennicutt (1998) conversion, corrected to the Chabrier IMF, and range from 0.4 to 6.6 $M_\odot$ yr^{-1} (uncorrected for dust extinction). We find winds with a FWHM^{broad} = 150–320 km s^{-1} which account for 30%–55% of the total Hα flux. These are somewhat less

b and *e* in both pointings, as well as both appearances of clump *g* in pointing 3. Clump apertures are defined as the 1σ extent of the best-fit Gaussians. Through a comparison with the F390W image, we additionally identify clumps *d* and *f* in pointing 2. These two clumps can also be seen in pointing 3, but there they only extend over one or two pixels, which introduces large uncertainties. Figure 9 shows the image-plane Hα emission

Figure 10. Integrated spectra for the clumps in pointing 2, all with robust wind detections. For every clump, the best-fit single component Gaussian model is shown in red in the left panel. The right panel shows the double component model in blue and the narrow and broad component are shown separately in gray. The residuals are shown at the bottom. From these, it becomes clear that a single Gaussian component fails to fit the broad wings of the Hα emission line; the double-component residual is significantly reduced at the location of the wings. The vertical dotted lines note the expected wavelength positions of the [N II] λ6548,6584 doublet.

(A color version of this figure is available in the online journal.)

Table 3
Clump Properties from the OSIRIS Data

Clump	$\Delta\chi^2$	$L_{\mathrm{H}\alpha}^{\mathrm{narrow}}$ (10^{41} erg s^{-1})	FWHM$^{\mathrm{narrow}}$ (km s^{-1})	FWHM$^{\mathrm{broad}}$ (km s^{-1})	Δv (km s^{-1})	$F^{\mathrm{broad}}/F^{\mathrm{tot}}$	$12 + \log(\mathrm{O/H})$
b	0.17	1.7 ± 0.1	81 ± 6	270 ± 33	23 ± 11	0.35 ± 0.12	8.02 ± 0.08
d	0.11	1.6 ± 0.1	99 ± 7	145 ± 30	-123 ± 20	0.28 ± 0.06	8.11 ± 0.07
e	0.50	4.0 ± 0.2	109 ± 4	315 ± 10	-23 ± 3	0.54 ± 0.05	8.28 ± 0.02
f	0.12	0.9 ± 0.1	84 ± 8	270 ± 41	6 ± 9	0.40 ± 0.17	8.08 ± 0.06
g	0.05	14.3 ± 0.3	160 ± 5				8.07 ± 0.06

Notes. Columns are the improvement in the reduced χ^2 between the single and double component Gaussian fits ($\sim$145 degrees of freedom), narrow-component de-lensed Hα luminosity, FWHM of the narrow and broad components, velocity offset between both components, the ratio of broad to total flux, and the oxygen abundance derived from the [N II]/Hα ratio. The quoted uncertainties are based on random errors; the metallicity calibration from Pettini & Pagel (2004) has a 0.2 dex systematic uncertainty and for the Hα luminosity one should take into account an additional systematic flux uncertainty of $\sim$30%.

broad than the FWHM$^{\mathrm{broad}} \sim 500$ km s^{-1} reported so far for a handful of more massive clumps in more massive $z \sim 1$–2 SFGs (Newman et al. 2012b; Wisnioski et al. 2012). This is expected given the positive correlation between wind velocity/FWHM and host galaxy stellar mass (Shapiro et al. 2009; Weiner et al. 2009; Newman et al. 2012a). Both the galaxy integrated mass and clump masses of RCSGA0327 are more than an order of magnitude lower than the $z \sim 2$ SFGs for which stellar winds have been resolved so far. Estimates of the mass-loading factors of outflows are highly uncertain due to the necessary assumptions on the geometry, rate, and physical extent of the outflow. Following the assumptions made in Newman et al. (2012a) for a warm ionized outflow with radially constant outflow velocity, we find mass-loading factors of one to four times the clump SFR.

Feedback from Active Galactic Nucleus (AGN) is a common explanation for the presence of broad emission lines. The outflows detected in RCSGA0327 are unlikely to be AGN powered for the following reasons: (1) the diagnostic Baldwin, Phillips, & Terlevich diagram (as derived from the long-slit NIRSPEC and FIRE data as well as *HST* grism data) does not show the extreme line ratios expected for an AGN origin of the emission lines (K. Whitaker et al. 2014, in preparation), (2) we see no evidence for point-source AGN activity in Mg II 2800 Å emission or *Chandra* X-ray data (J. R. Rigby et al. 2014, in preparation), and (3) the broad component is spatially extended and it can be identified for multiple spatial pixels within the clump apertures. Unfortunately, the OSIRIS data have insufficient S/N to fit a double-component Gaussian model to individual spatial pixels and spatially map the strength of the outflow. We note that the kinematic maps presented in Section 3.1 result from single Gaussian fits. The presence of outflows will not affect the velocity map, since the velocity shift between the single best-fit model and the narrow component of a double model is negligible. The velocity dispersion is overestimated by 30%–40% in the clump regions.

Newman et al. (2012a) present evidence for a strong dependence of the strength of outflows on the star formation surface density (Σ_{SFR}) of the galaxy or clump from which they originate. They propose a threshold of $\Sigma_{\mathrm{SFR}} > 1\ M_\odot$ yr^{-1} kpc^{-2} to power a strong wind at $z \sim 2$, i.e., where the broad component accounts for at least one third of the total flux. This is an order of magnitude higher than the star formation surface density threshold found in the local universe (Heckman et al. 2002). Since gravitational lensing conserves surface brightness, Σ_{SFR} for the clumps in RCSGA0327 can be estimated in the image plane from the observed narrow-component Hα luminosity and
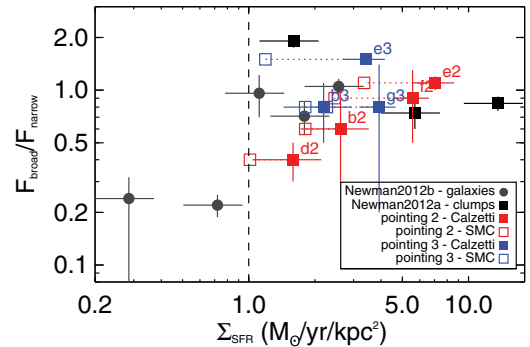
Figure 11. Dependence of the outflow strength, characterized as the fraction of Hα flux contained in the broad vs. narrow component, on star formation surface density. The gray circles present stacked results for $z \sim 2$ SFGs from the SINS survey (Newman et al. 2012a). The black squares correspond to outflows detected for three individual clumps within two of the most massive SINS galaxies (Newman et al. 2012b). The clumps in RCSGA0327 are shown in red and blue for pointing 2 and 3, respectively. The clump SFR is derived from the narrow-component Hα luminosity and corrected for dust extinction using the SED-derived reddening $E(B - V)_s$ from either the Calzetti (filled squares) or the SMC (open squares) dust extinction law. We assume no additional extinction toward the nebular emission lines.

(A color version of this figure is available in the online journal.)

the size of the OSIRIS clump apertures. A dust correction is applied based on the SED-derived reddening, using either the Calzetti or SMC extinction law and assuming that the nebular emission lines and stellar continuum suffer the same amount of extinction (see Section 4.5). Figure 11 shows that the clumps all have high star formation surface densities significantly above the proposed threshold $\Sigma_{\mathrm{SFR}} > 1\ M_\odot$ yr^{-1} kpc^{-2}.

The S/N of the OSIRIS observations is insufficient to detect [N II] emission in most individual spatial pixels, but the lines are detected at S/N $>$ 2 in the integrated spectra of all clumps in pointing 2, as well as clumps e and g in pointing 3. We measure the [N II] flux by fitting a multi-component Gaussian model to Hα and both [N II] lines using MPFITFUN. We fix the linewidths to a common value and constrain the ratio of the [N II] doublet to its theoretical value of 3.071 (Storey & Zeippen 2000). For pointing 2, a second broad component is included for all lines, also with a common linewidth. Additionally, we constrain the flux ratio of the narrow and broad component of each line to a common value. We estimate the metallicity of each clump from the ratio of [N II] λ6585 to Hα, the N2 index, as empirically calibrated by Pettini & Pagel (2004), and report the results in Table 3. The calibration of strong-line metallicity indicators remains uncertain at high redshift (e.g., Kewley &

Ellison 2008; Wuyts et al. 2012b), but here we are mainly concerned with the relative variations in abundance among the clumps. The Pettini & Pagel (2004) calibration has a systematic uncertainty of 0.2 dex.

4.5. Clumps in FIRE and NIRSPEC

This section explores additional information that can be learned from the long-slit NIR spectra taken with Magellan/FIRE for clumps *u* and *b*2 and Keck/NIRSPEC for clumps *u* and *e*2 presented in Sections 2.3 and 2.4.

4.5.1. Extinction

Following R11, we measure extinctions from the NIRSPEC spectra of clumps *u* and *e*2 from the Hβ/Hγ ratio, which is the brightest pair of Balmer lines covered within a single grating setting. Using the Calzetti extinction law, the measured reddening is $E(B - V)_g = 0.34 \pm 0.10$ for clump *u* and $E(B - V)_g = 0.23 \pm 0.09$ for clump *e*2. This is a more accurate measurement than in R11, mostly because we have switched to fitting a common continuum level and linewidth for all lines in each grating setting. For FIRE, we can use both the Hα/Hβ and Hβ/Hγ ratios. We find $E(B - V)_g^{\alpha\beta} = 0.38 \pm 0.04$ and $E(B - V)_g^{\beta\gamma} = 0.32 \pm 0.30$ for clump *u* and $E(B - V)_g^{\alpha\beta} = 0.16 \pm 0.03$ and $E(B - V)_g^{\beta\gamma} = 0.07 \pm 0.15$ for clump *b*2. For clump *u*, the reddening estimates derived from NIRSPEC and FIRE are consistent.

We can compare these reddening measures with the reddening of the stellar light as derived from the best-fit SED model and reported in Table 2. This comparison is visualized in the bottom-left panel of Figure 13 and suggests there is no need for additional extinction toward the ionized gas when the Calzetti extinction law is applied, while $E(B - V)_g$ is significantly higher than $E(B - V)_s$ for the SMC law.

4.5.2. Electron Density

We use the [O II] λ3727 doublet to constrain the electron density, using the task *stsdas.analysis.temden* in IRAF[10] with $T_e = 10^4$ K, as done in R11. From the NIRSPEC data, a line flux ratio of $f(3726/3729) = 1.19 \pm 0.07$ translates to an electron density $n_e = 600 \pm 100$ cm^{-3} for clump *e*2; for clump *u* we find $f(3726/3729) = 0.84 \pm 0.03$ and $n_e = 180 \pm 35$ cm^{-3}. From the FIRE data, we find $f(3726/3729) = 0.84 \pm 0.08$ and $n_e = 180 \pm 90$ cm^{-3} for clump *b*2 and $f(3726/3729) = 1.01 \pm 0.13$ and $n_e = 370 \pm 150$ cm^{-3} for clump *u*.

4.5.3. Metallicity

We estimate the metallicity from the Hα and [N II] emission line fluxes measured in the NIRSPEC and FIRE spectra. Using the third-order polynomial fit of Pettini & Pagel (2004), we infer a metallicity of $12 + \log(O/H) = 8.16 \pm 0.02$ for clump *u* and $12 + \log(O/H) = 8.34 \pm 0.02$ for clump *e*2 from the NIRSPEC data. From FIRE, we derive a metallicity of $12 + \log(O/H) = 8.16 \pm 0.02$ for clump *u* and $12 + \log(O/H) = 8.12 \pm 0.02$ for clump *b*2. These estimates are consistent with the OSIRIS results presented in Section 4.4, as can also be seen in the bottom-right panel of Figure 13.

---

[10] IRAF is distributed by the National Optical Astronomy Observatories, which are operated by the Association of Universities for Research in Astronomy, Inc., under cooperative agreement with the National Science Foundation.
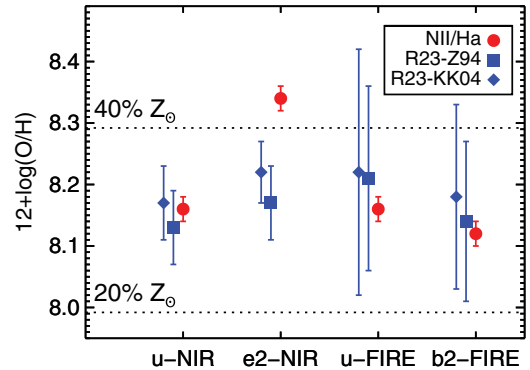

Figure 12. Comparison of metallicity indicators for the NIRSPEC and FIRE spectra. We show metallicities derived from the N2 index, log([N II]λ6584/Hα), as calibrated by Pettini & Pagel (2004; red circles), as well as metallicities derived from the R_{23} index, $\log R_{23} = \log[([O II] \lambda3727 + [O III] \lambda4959 + [O III] \lambda5007)/H\beta]$, as calibrated by Zaritsky et al. (1994; blue squares) and Kobulnicky & Kewley (2004; blue diamonds). The latter two have been converted to the N2 calibration of Pettini & Pagel (2004) with the conversions from Kewley & Ellison (2008). Only statistical uncertainties are shown; the indicators each have a systematic uncertainty of at least 0.2 dex.

(A color version of this figure is available in the online journal.)

The extended wavelength coverage of the NIRSPEC and FIRE spectra includes additional lines that can be used to estimate metallicity. One needs to keep in mind the significant offsets between different strong-line indicators, which need to be converted to the same base calibration before any comparison can be made (Kewley & Ellison 2008). Additionally, emission line fluxes need to be corrected for dust extinction when the strong-line indicator spans a large wavelength range. The R_{23} index, $\log R_{23} = \log[([O II] \lambda3727 + [O III] \lambda4959 + [O III] \lambda5007)/H\beta]$, is commonly used in the literature. This indicator is double valued with a low and high metallicity result for every value of R_{23}. Using the [N II]/[O II] flux ratio to distinguish between both metallicity branches (Kewley & Ellison 2008), we find that all clumps fall on the upper branch. We proceed to use the upper branch R_{23} calibration from Zaritsky et al. (1994) as well as Kobulnicky & Kewley (2004) and convert both results to our base metallicity calibration of [N II/Hα] from Pettini & Pagel (2004). The results for all clumps are shown in Figure 12. Only statistical uncertainties are shown; the indicators each have a systematic uncertainty of at least 0.2 dex. The larger uncertainties for the R_{23} indicators originate from the propagation of the uncertainty in the reddening. We see a general agreement between metallicity indicators, except for clump *e*2, where the metallicity derived from the [N II]/Hα ratio is larger by ~0.15 dex. This offset falls within the significant systematic uncertainties involved in the comparison of metallicity indicators, but given the agreement between the N2 and R_{23} index for the other clumps, it does suggest that the [N II]/Hα ratio of clump *e*2 is elevated. This agrees with the higher electron density measured for this clump, which results in an increased rate of collisional excitation. Additionally, the galactic wind detected for clump *e* could drive shock excitation. At high redshift ($z > 1.5$), the presence of slow shocks mimics a higher metallicity starburst (Kewley et al. 2013).

4.5.4. Outflows

The FIRE spectrum of clump *b*2 and the NIRSPEC spectra of clump *e*2 show an outflow consistent with the OSIRIS results. No outflow is detected in the FIRE or NIRSPEC spectra of clump *u*.
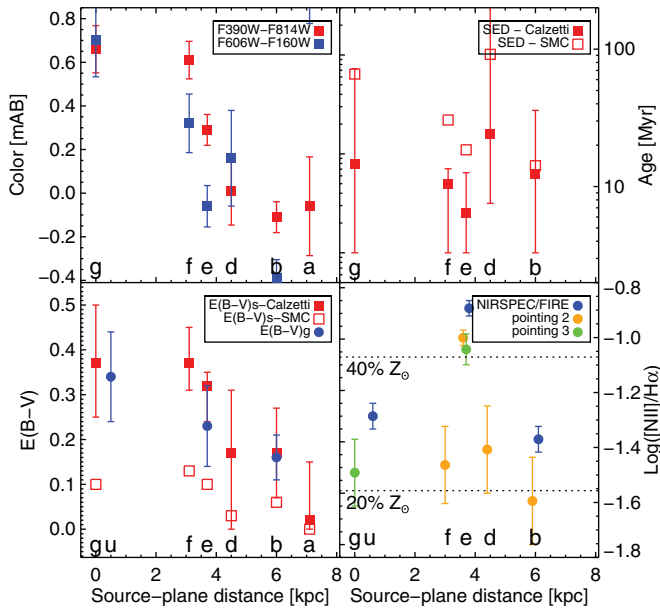
Figure 13. Radial variation of clump properties. The *x*-axis corresponds to the projected source-plane distance from each clump to clump *g*. Red and blue symbols denote results from the SED fit with the Calzetti and SMC extinction laws, respectively. Orange and green symbols correspond to OSIRIS results and blue symbols show long-slit spectroscopy with NIRSPEC and FIRE. Error bars only reflect statistical uncertainties. Top left: F390W–F814W rest-frame UV color; top right: stellar age; bottom left: reddening from the SED fit and from the Balmer ratio; bottom right: metallicity.

(A color version of this figure is available in the online journal.)

4.6. Radial Variation of Clump Properties

Any trends in clump properties with respect to their location within the galaxy can provide additional constraints on the clump origin. No correlation is expected among the properties of separate interacting components. Since there is no clear definition of the galaxy center for RCSGA0327, we adopt the position of clump *g*, which is the brightest clump and corresponds to a strong peak in stellar mass surface density (see Section 5). For each clump, the projected distance to clump *g* is measured in the reconstructed source-plane images. The top left panel of Figure 13 shows the rest-frame $U - V$ color F606W–F160W as well as a measure of the UV slope from the F390W–F814W color. We see a slight radial trend, where clumps become redder by 0.5–1 mag when moving east from clump *a* toward clump *g*. Such color trends have been interpreted as evidence for a radial age trend, confirming a picture of radial migration of clumps formed through gravitational collapse of a turbulent disk (Guo et al. 2012). However, rest-frame UV color is governed by a degeneracy among age, metallicity, and dust extinction and a color trend can be caused by a trend in any of these parameters. The top right panel shows the stellar age as derived from the SED using both the Calzetti and SMC extinction laws (filled and open red squares, respectively). The stellar age remains roughly constant across the clumps, within the significant uncertainties. There is some evidence for an increase in reddening toward clump *g*, as shown in the bottom left panel. Some correlation between color and reddening is expected from the SED modeling, but the trend is confirmed by the reddening of the ionized gas derived from the NIRSPEC and FIRE spectra (blue filled circles).

The bottom right panel of Figure 13 shows the [N II]/ Hα ratio, as measured in OSIRIS, as well as the NIRSPEC

and FIRE spectra. The [N II]/Hα ratio shows a mostly flat gradient across the clumps, with the exception of clump *e*. We have discussed in Section 4.5 how the elevated [N II]/ Hα ratio for this clump is likely due to an increased electron density and/or shock excitation in the outflow. Based on the R_{23} indicator, the metallicity of clump *e* agrees with the other clumps. A flat metallicity gradient supports the scenario of an ongoing interaction within the system. In merger simulations, galaxy metallicity gradients are found to flatten as the merger progresses and low-metallicity gas is transported from the outskirts of the interacting galaxies to the central region (Rupke et al. 2010a). This has been seen in local close-pair spiral galaxies (Kewley et al. 2010; Rupke et al. 2010b) and local LIRGs (Rich et al. 2012). IFS studies of both lensed and non-lensed $z \sim 2$ SFGs are also finding flatter or even inverted metallicity gradients in interacting systems, although samples are still small (Jones et al. 2013).

4.7. Clump Scaling Relations

The five well-measured clumps in RCSGA0327 present a sizeable contribution to the current sample of 40 star-forming regions in $z \sim 2$ SFGs with reliable Hα measurements: (1) five clumps from three $z \sim 2$ SINS galaxies (Genzel et al. 2011), (2) eight clumps from three massive SFGs at $z \sim 1.3$ from the WiggleZ survey (Wisnioski et al. 2012), (3) eight clumps from four lensed galaxies at $z = 1.6$–2.6 (Jones et al. 2010), (4) nine clumps from four Hα-selected galaxies at $z = 1.4$ and $z = 2.2$ from HiZELS (Swinbank et al. 2012), and (5) 10 clumps in three submillimeter-selected galaxies (SMGs) at $z = 1.4$–2.4 (Menéndez-Delmestre et al. 2013). Additionally, Livermore et al. (2012) use *HST*/WFC3 narrowband imaging centered on Hα to study clump sizes and luminosities in an additional eight lensed galaxies at $z = 1$–1.5; they have no kinematic information. Figure 14 compares Hα luminosity (uncorrected for dust extinction), size, and velocity dispersion measurements for the sample of high-*z* clumps with local scaling relations among these parameters taken from Wisnioski et al. (2012). These authors have remeasured all clump sizes consistently with 2D elliptical Gaussian fits. The size-luminosity relation in the left panel clearly shows how the three lensing studies (Jones et al. 2010; Livermore et al. 2012, and this work) probe clump sizes up to an order of magnitude smaller than what can be resolved in non-lensed studies. The clumps in RCSGA0327 are broadly consistent with the other high-*z* clumps and lie roughly two orders of magnitude above the local luminosity-size scaling relation. As was first pointed out by Livermore et al. (2012), the offset seems to increase with redshift. These authors found correlations between clump SFR surface density and the SFR surface densities and gas surface densities of the host galaxies. As such, high-redshift clumps appear to be scaled-up analogs of local H II regions, simply bigger and brighter because of the increasing gas fractions in high-*z* SFGs.

It is worth asking whether the dynamical state of the host galaxy plays a role in determining the clump SFR surface densities. In the local universe, giant H II regions found in interacting systems (shown with black filled diamonds) show systematically higher SFR surface densities compared with giant H II regions in local spirals (open diamonds). At high redshift, we do not see elevated SFR surface densities for clumps within kinematically classified interacting systems (RCSGA0327, two lensed galaxies from Jones et al. 2010, one HiZELS source from Swinbank et al. 2012, and three SMGs studied by Menéndez-Delmestre et al. 2013). It would be very valuable to obtain direct gas
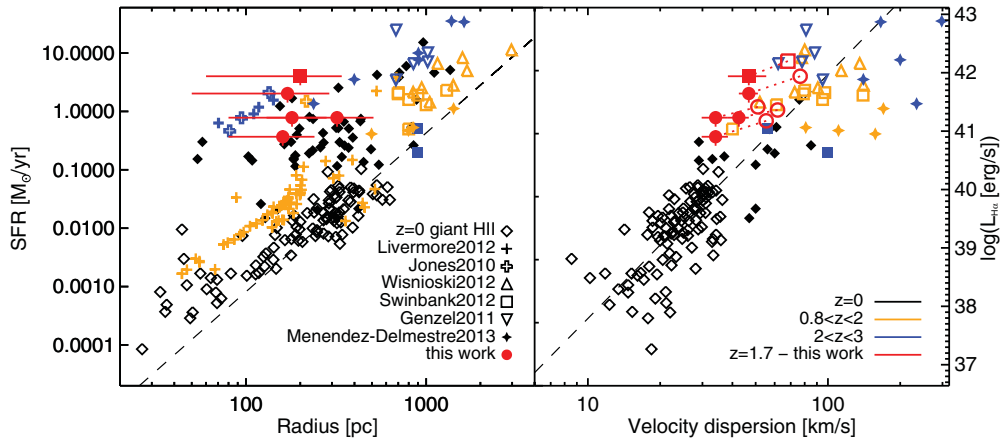
Figure 14. Scaling relations between Hα luminosity and size (left) or velocity dispersion (right) for local and high-redshift star-forming clumps. The dashed black lines display the best-fit scaling relations from Wisnioski et al. (2012). The local sample consists of giant H II regions in local spirals (rotating disks; Gallagher & Hunter 1983; Arsenault & Roy 1988; Rozas et al. 2006) and giant H II regions in local ULIRGs (interacting systems; Bastian et al. 2006; Monreal-Ibero et al. 2007; Rodríguez-Zaurín et al. 2011). We use open and closed black diamonds to differentiate between these kinematic classifications. The high-z clumps come from six different studies mentioned in the text and the legend. We have color coded them by redshift to look for redshift evolution of the scaling relations: $0.8 < z < 2$ (orange) and $2 < z < 3$ (blue). Open and closed symbols are again used to differentiate between kinematically classified rotating disks and interacting systems. The lensed galaxies from Livermore et al. (2012) do not have kinematic information and are shown with plus symbols. Neither Livermore et al. (2012) nor Jones et al. (2010) report velocity dispersion measurements for their clumps, which are therefore not included in the right panel. Results from the narrow-component Hα emission line profile for the clumps in RCSGA0327 are shown with filled red circles and a filled red square for clump g. The open red symbols in the right panel show the overestimate of both Hα luminosity and linewidth when fitting the line profiles with a single Gaussian, not taking into account the broad underlying wind component.

(A color version of this figure is available in the online journal.)

measurements of these systems to clarify the connections among gas surface density, star formation surface density, and galaxy kinematics.

A few caveats should be kept in mind in the analysis of the scaling relations presented above. First, the high-redshift clumps form by no means a uniformly selected sample, but span a large range of host galaxy selection and integrated properties. Second, the Hα luminosities in Figure 14 have not been corrected for dust extinction. This is mostly driven by the lack of reliable extinction estimates, especially on the scale of the individual clumps. Variations in dust extinction with redshift or host galaxy properties could have a significant effect on the scatter in these scaling relations. Finally, not taking into account a broad underlying wind component when fitting the Hα emission line profile will lead to overestimates of both the Hα luminosity and velocity dispersion of clumps. This is illustrated for RCSGA0327 with the open and closed red symbols in the right panel of Figure 14.

5. SPATIALLY RESOLVED SED MODELING

The stellar mass surface density of a galaxy holds crucial information regarding the physical origin of its individual star-forming regions. When clumps correspond to separate interacting components, one can expect a well-established older stellar population underlying their strong rest-frame UV presence caused by the recent star formation triggered in the interaction. In contrast, clumps formed through gravitational collapse of a gas-rich, turbulent disk are too short lived to build up a significant population of old stars. Dynamical friction against the underlying galaxy disk and clump-clump interactions cause the clumps to spiral inward and coalesce into the galaxy center on timescales ∼300–500 Myr (e.g., Dekel & Krumholz 2013). The detection of strong outflows originating from clumps in RCSGA0327 and other studies (Genzel et al. 2011; Newman et al. 2012b; Wisnioski et al. 2012) could disrupt the clumps on even shorter timescales (Genel et al. 2012). Thus,

while clumps dominate the galaxy morphology in rest-frame UV light, which mostly traces newly formed O and B stars, they become much less prominent at rest-frame optical wavelengths. Along these lines, Wuyts et al. (2012c) have recently quantified the reduced contribution of clumps to stellar mass maps of clumpy galaxies at $0.5 < z < 2.5$ in the CANDELS fields based on spatially resolved SED modeling. Here, we perform similar modeling for RCSGA0327.

We model the counter image to obtain a full image of the source-plane galaxy without the contamination of the cluster galaxies that fall on top of image 3. Following the procedure outlined in Wuyts et al. (2012c), we PSF-match the different WFC3 images to the broadest F160W PSF and group pixels using 2D Voronoi binning (Cappellari & Copin 2003) to achieve $S/N \geqslant 10$ in this band. For the SED fit, we use the default assumptions described in Section 4.2 for the modeling of the clumps: BC03 models, Calzetti dust extinction, Chabrier IMF, 0.2–0.4 $Z_\odot$ metallicity, exponentially decreasing SFHs with $\log(\tau) \geqslant 8.5$, and no age restriction. Different modeling assumptions will generally affect only the absolute value of the derived stellar population parameters and here we are mostly interested in the relative variation of these parameters across the galaxy. As discussed in Section 4.2, the F098M and F125W filters can be heavily contaminated by line emission and are excluded from the SED fit. As a consistency check, adding the stellar mass of all the Voronoi bins returns a total galaxy mass within 0.1 dex of the stellar mass derived from the galaxy-integrated photometry; Wuyts et al. (2012c) found a scatter of 0.08 dex in their comparison of integrated and resolved stellar masses for $1.5 < z < 2.5$ CANDELS galaxies.
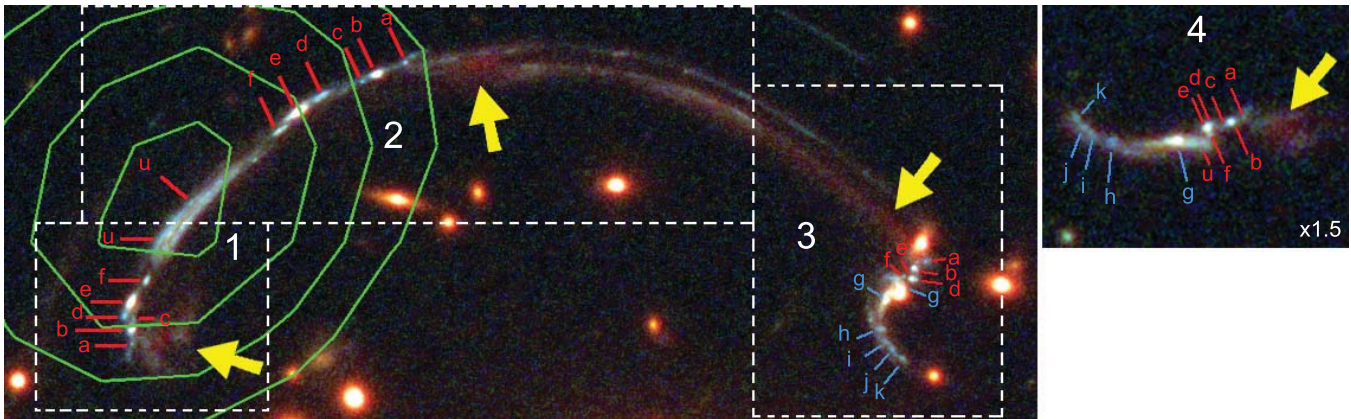
The top row of Figure 15 shows source-plane maps of the F606W and F160W WFC3 images, which roughly correspond to rest-frame 2800 Å and 5500 Å. Clumps g, e, and b are shown with black crosses, from left to right. The clumps become less pronounced at redder wavelengths, but clump g still shows up strongly in the F160W image. This agrees with its significant presence in the stellar mass surface density map in the bottom
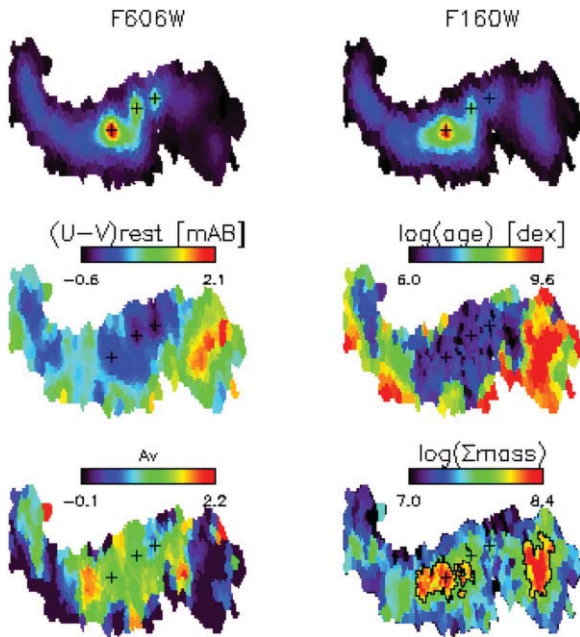
Figure 15. Source-plane images of RCSGA0327 based on the counter image: surface brightness distributions in the F606W and F160W bands (corresponding to rest-frame 2800 Å and 5500 Å), rest-frame $U - V$ color map based on F814W–F160W, stellar age, dust extinction, and stellar mass surface density. Clumps g, e, and b are marked by black crosses, from left to right. The contour on the stellar mass surface density map corresponds to $\log(\Sigma_{M*}) = 8.0$.

(A color version of this figure is available in the online journal.)

right panel of Figure 15. Based on this map, the other large mass concentration in RCSGA0327 lies on its western edge, to the right of all the clumps. This region has not been discussed so far, since it was not detected in Hα emission.[11] It is very red in the false-color image presented in Figure 1 and the rest-frame $U - V$ color map in Figure 15. Based on the stellar age and dust extinction maps, the red color is attributed to an old stellar population and not to dust-obscured star formation. This agrees with the non-detection of this region in the OSIRIS

---

[11] Due to the non-detection in the OSIRIS data, we have no spectroscopic confirmation of the redshift of this red component. However, given that it is multiply imaged together with the rest of the system, the details of the lens modeling restrict its redshift to within ~1000 km s^{-1} of the systemic velocity.

data and recent *Herschel* PACS/SPIRE observations (Figure 16; J.R.R.Rigby et al. 2014, in preparation).

Out to an isophote of $\log(\Sigma_{M*}) \geqslant 8.0$ (the black contour on top of the stellar mass surface density map in Figure 15), clump g and the red western region each contain ~1.2×10^9 $M_\odot$ or ~20% of the galaxy-integrated stellar mass in RCSGA0327. Within this contour, the western mass component has an intrinsic SFR of 0.5 $M_\odot$ yr^{-1}, which puts it ~2σ below the main sequence at $z = 2$.

6. SUMMARY OF OBSERVATIONAL RESULTS AND DISCUSSION

We have presented a detailed analysis of the kinematics, spatially resolved stellar population parameters, and clump properties of RCSGA0327 based on multi-wavelength *HST*/ WFC3 imaging and AO-assisted OSIRIS IFS data. The main results are summarized below.

1. The kinematical analysis of the OSIRIS data strongly suggests an ongoing interaction, which has caused a large tidal tail extending from clump g toward the northeast. Velocity dispersion peaks between the clumps could arise from high turbulence due to the interaction or overlapping Hα emission along the line of sight.

2. We have identified seven individual star-forming regions in the WFC3 imaging with diameters ranging from 300–600 pc. SED modeling of the clump photometry predicts stellar masses 10^7–5×10^8 $M_\odot$, young ages of ~5–100 Myr, and low reddening $E(B - V) < 0.4$. The steeper SMC extinction law is preferred over the default Calzetti law to avoid unphysical high clump SFRs compared with the Hα-derived values as well as the galaxy-integrated SFR.

3. RCSGA0327 is the lowest mass high-z SFG to date with resolved outflows. We find broad underlying wind components in the Hα emission line profile of four clumps, contributing on average ~40% to their total Hα flux. The SFR surface densities of these clumps all fall above the high-z threshold of $\Sigma_{SFR} > 1$ $M_\odot$ yr^{-1} kpc^{-2} to power strong winds.

4. We find a radial gradient in rest-frame UV color of the clumps across the galaxy, which we infer to be caused by a gradient in reddening. The stellar age of the clumps,

Figure 16. Same as Figure 1. The green lines correspond to the 1.5σ, 2.0σ, 2.5σ, and 3.0σ contours of the PACS 100 μm image, which represents the best combination of S/N spatial resolution and sensitivity to re-processed dust emission out of the available far-infrared imaging. The yellow arrows indicate the second, red mass component in each of the four images of the source. The *Herschel* data make clear that the bulk of the long-wavelength emission is associated with clump u and that there is no emission associated with this second mass concentration.

(A color version of this figure is available in the online journal.)

although uncertain in absolute value, remains roughly constant. We find a flat metallicity gradient, as expected for an interacting system.

5. The clumps in RCSGA0327 agree with the size–luminosity and dispersion–luminosity correlations inferred from earlier lensed and non-lensed studies of high-z clumps. Kinematical classification of the host galaxy as an interacting system does not result in higher clump SFR surface densities, unlike what has been seen for local giant H II regions.

6. Stellar mass surface density maps based on spatially resolved SED modeling suggest an established stellar population at the location of clump g and a second mass component at the western edge of the galaxy. Both contain $\sim$20% of the total stellar mass of the system. The western mass component is not detected in Hα or far-infrared emission.

In contrast to most clumpy $z \sim 2$ SFGs that have been studied in detail so far, RCSGA0327 does not agree with a single turbulent rotating disk where clumps have formed through gravitational collapse. The system is undergoing an interaction, which has boosted the specific SFR to a factor of 3 above the main sequence at $z \sim 2$. The enhanced star formation is localized in multiple compact star-forming regions with high star formation surface densities and signatures of outflows. Such off-center areas of enhanced star formation activity have also been seen in local mergers, such as the Antennae galaxies (Whitmore & Schweizer 1995; Karl et al. 2010). The red mass component at the western edge of the system does not show significant dust-obscured or unobscured star formation. As such, this component must have been gas-poor before the start of the interaction, such that no new burst of star formation could be triggered. This would also explain why we do not see a tidal tail originating from this component. We note that for clump g, the young stellar age derived from the SED fit is only relevant for the current star formation episode triggered by the interaction and does not contradict the interpretation of this clump as an established stellar population.

As a roughly equal mass, mixed merger of one gas-rich and one gas-poor component, RCSGA0327 is not a common occurrence. Both theoretical and observational estimates of merger rates find that only $\sim$10% of $z \sim 2$ galaxies at $10^9 \, M_\odot$ are currently undergoing an interaction (Conselice et al. 2003; Guo & White 2008). However, the number of mergers involving one or both components that are gas poor is significantly less than that, given the overall increase in galaxy gas fraction with redshift. Lin et al. (2008) find that 24% of mergers are mixed at $z \sim 1.1$ based on galaxy pair counts in the DEEP2 Redshift Survey. On top of that, the stellar mass estimate of $\sim$1.2 × $10^9 \, M_\odot$ for the gas-poor component in RCSGA0327 is unusually low, as can be seen for example from the mass distribution of passive galaxies at $1.4 < z < 2.5$ in GOODS-South (Figure 3, Lee et al. 2013).

Merger simulations mostly focus on the low-redshift universe and have so far failed to take into account the different nature of $z \sim 2$ SFGs as evidenced by their clumpy morphology, higher gas fractions, and stronger turbulence. Recent studies have shown that turbulence and clumpiness have a substantial effect in mergers of present-day spirals with just a few percent of gas, causing significant differences in the SFH during the interaction (Teyssier et al. 2010; Saitoh et al. 2009). The effect could presumably be more dramatic in high-redshift mergers involving high gas fractions. Bournaud et al. (2011) present the first wet merger simulations involving two realistic massive, gas-rich, clumpy disks. Such work needs to be extended to lower

mass galaxies, as well as mixed and dry mergers involving early-type, gas-poor components.

To finish, we would like to stress two main points that were instrumental in obtaining a full understanding of the physical nature of RCSGA0327. The first point concerns the combination of IFS data with high-resolution rest-frame UV to optical imaging. The kinematics of the ionized gas and the morphology of current star formation derived from IFS data need to be complemented with an understanding of the underlying stellar population derived from spatially resolved SED modeling. In the case of RCSGA0327, the gas-poor component in the interaction only became apparent in the stellar mass surface density maps. Secondly, the analysis presented here would not have been possible without the lensing magnification, which allowed a high-resolution velocity profile and detailed measurements of multiple <1 kpc size clumps. The resulting unprecedented view of a rare ongoing interaction at $z \sim 2$ shows the promise of detailed study of individual systems to aid and constrain theoretical efforts toward understanding galaxy formation and evolution.

REFERENCES

Adamo, A., Östlin, G., Bastian, N., et al. 2013, ApJ, 766, 105
Arsenault, R., & Roy, J.-R. 1988, A&A, 201, 199
Barro, G., Faber, S. M., Perez-Gonzalez, P. G., et al. 2013, ApJ, 765, 104
Bastian, N., Emsellem, E., Kissler-Patig, M., & Maraston, C. 2006, A&A, 445, 471
Bournaud, F., Chapon, D., Teyssier, R., et al. 2011, ApJ, 730, 4
Bournaud, F., & Elmegreen, B. G. 2009, ApJL, 694, L158
Bournaud, F., Elmegreen, B. G., & Elmegreen, D. M. 2007, ApJ, 670, 237
Bruzual, G., & Charlot, S. 2003, MNRAS, 344, 1000
Calzetti, D., Armus, L., Bohlin, R. C., et al. 2000, ApJ, 533, 682
Cappellari, M., & Copin, Y. 2003, MNRAS, 342, 345
Chabrier, G. 2003, PASP, 115, 763
Conselice, C. J., Bershady, M. A., Dickinson, M., & Papovich, C. 2003, AJ, 126, 1183
Conselice, C. J., Yang, C., & Bluck, A. F. L. 2009, MNRAS, 394, 1956
Daddi, E., Bournaud, F., Walter, F., et al. 2010, ApJ, 713, 686
Daddi, E., Dickinson, M., Morrison, G., et al. 2007, ApJ, 670, 156
Davies, R. I. 2007, MNRAS, 375, 1099
Davies, R., Förster Schreiber, N. M., Cresci, G., et al. 2011, ApJ, 741, 69

Dekel, A., & Krumholz, M. R. 2013, MNRAS, 432, 455
Dekel, A., Sari, R., & Ceverino, D. 2009, ApJ, 703, 785
Duc, P.-A., Brinks, E., Springel, V., et al. 2000, AJ, 120, 1238
Elbaz, D., Daddi, E., Le Borgne, D., et al. 2007, A&A, 468, 33
Elmegreen, B. G., Elmegreen, D. M., Fernandez, M. X., & Lemonias, J. J. 2009, ApJ, 692, 12
Elmegreen, D. M., Elmegreen, B. G., Ravindranath, S., & Coe, D. A. 2007, ApJ, 658, 763
Epinat, B., Amram, P., Balkowski, C., & Marcelin, M. 2010, MNRAS, 401, 2113
Epinat, B., Tasca, L., Amram, P., et al. 2012, A&A, 539, A92
Förster Schreiber, N. M., Genzel, R., Bouché, N., et al. 2009, ApJ, 706, 1364
Förster Schreiber, N. M., Shapley, A. E., Genzel, R., et al. 2011, ApJ, 739, 45
Franx, M., van Dokkum, P. G., Schreiber, N. M. F., et al. 2008, ApJ, 688, 770
Gallagher, J. S., & Hunter, D. A. 1983, ApJ, 274, 141
Genel, S., Naab, T., Genzel, R., et al. 2012, ApJ, 745, 11
Genzel, R., Newman, S., Jones, T., et al. 2011, ApJ, 733, 101
Gilbank, D. G., Gladders, M. D., Yee, H. K. C., & Hsieh, B. C. 2011, AJ, 141, 94
Griffiths, R. E., Casertano, S., Ratnatunga, K. U., et al. 1994, ApJL, 435, L19
Guo, Q., & White, S. D. M. 2008, MNRAS, 384, 2
Guo, Y., Giavalisco, M., Ferguson, H. C., Cassata, P., & Koekemoer, A. M. 2012, ApJ, 757, 120
Heckman, T. M., Norman, C. A., Strickland, D. K., & Sembach, K. R. 2002, ApJ, 577, 691
Hibbard, J. E., Guhathakurta, P., van Gorkom, J. H., & Schweizer, F. 1994, AJ, 107, 67
Hopkins, P. F., Bundy, K., Croton, D., et al. 2010, ApJ, 715, 202
Immeli, A., Samland, M., Gerhard, O., & Westera, P. 2004a, A&A, 413, 547
Immeli, A., Samland, M., Westera, P., & Gerhard, O. 2004b, ApJ, 611, 20
Jones, T., Ellis, R. S., Richard, J., & Jullo, E. 2013, ApJ, 765, 48
Jones, T. A., Swinbank, A. M., Ellis, R. S., Richard, J., & Stark, D. P. 2010, MNRAS, 404, 1247
Karl, S. J., Naab, T., Johansson, P. H., et al. 2010, ApJL, 715, L88
Kaviraj, S., Cohen, S., Windhorst, R. A., et al. 2013, MNRAS, 429, L40
Kelson, D. D. 2003, PASP, 115, 688
Kennicutt, R. C., Jr. 1998, ARA&A, 36, 189
Kereš, D., Katz, N., Fardal, M., Davé, R., & Weinberg, D. H. 2009, MNRAS, 395, 160
Kereš, D., Katz, N., Weinberg, D. H., & Davé, R. 2005, MNRAS, 363, 2
Kewley, L. J., Dopita, M. A., Leitherer, C., et al. 2013, ApJ, 774, 100
Kewley, L. J., & Ellison, S. L. 2008, ApJ, 681, 1183
Kewley, L. J., Rupke, D., Zahid, H. J., Geller, M. J., & Barton, E. J. 2010, ApJL, 721, L48
Kobulnicky, H. A., & Kewley, L. J. 2004, ApJ, 617, 240
Koekemoer, A. M., Fruchter, A. S., Hook, R., & Hack, W. 2002, in HST Calibration Workshop, (Baltimore, MD: STScI), 337
Kriek, M., van Dokkum, P. G., Labbé, I., et al. 2009, ApJ, 700, 221
Krist, J. E., Hook, R. N., & Stoehr, F. 2011, Proc. SPIE, 8127, 81270J
Kronberger, T., Kapferer, W., Schindler, S., & Ziegler, B. L. 2007, A&A, 473, 761
Larkin, J., Barczys, M., Krabbe, A., et al. 2006, Proc. SPIE, 6269, 42
Law, D. R., Steidel, C. C., Erb, D. K., et al. 2009, ApJ, 697, 2057
Lee, B., Giavalisco, M., Williams, C. C., et al. 2013, ApJ, 774, 47
Lin, L., Patton, D. R., Koo, D. C., et al. 2008, ApJ, 681, 232
Livermore, R. C., Jones, T., Richard, J., et al. 2012, MNRAS, 427, 688
Lotz, J. M., Jonsson, P., Cox, T. J., et al. 2011, ApJ, 742, 103
Markwardt, C. B. 2009, in ASP Conf. Ser. 411, Astronomical Data Analysis Software and Systems XVIII, ed. D. A. Bohlender, D. Durand, & P. Dowler (San Francisco, CA: USA), 251
Menéndez-Delmestre, K., Blain, A. W., Swinbank, M., et al. 2013, ApJ, 767, 151
Mihos, J. C., & Bothun, G. D. 1998, ApJ, 500, 619

Monreal-Ibero, A., Colina, L., Arribas, S., & García-Marín, M. 2007, A&A, 472, 421
Naab, T., & Burkert, A. 2003, ApJ, 597, 893
Naab, T., Johansson, P. H., Ostriker, J. P., & Efstathiou, G. 2007, ApJ, 658, 710
Nesvadba, N. P. H., Lehnert, M. D., Eisenhauer, F., et al. 2006, ApJ, 650, 661
Newman, S. F., Genzel, R., Forster-Schreiber, N., et al. 2012a, ApJ, 761, 43
Newman, S. F., Shapiro Griffin, K., Genzel, R., et al. 2012b, ApJ, 752, 111
Noeske, K. G., Weiner, B. J., Faber, S. M., et al. 2007, ApJL, 660, L43
Noguchi, M. 1999, ApJ, 514, 77
Peng, C. Y., Ho, L. C., Impey, C. D., & Rix, H.-W. 2010, AJ, 139, 2097
Pettini, M., & Pagel, B. E. J. 2004, MNRAS, 348, L59
Prevot, M. L., Lequeux, J., Prevot, L., Maurice, E., & Rocca-Volmerange, B. 1984, A&A, 132, 389
Reddy, N. A., Steidel, C. C., Fadda, D., et al. 2006, ApJ, 644, 792
Rich, J. A., Torrey, P., Kewley, L. J., Dopita, M. A., & Rupke, D. S. N. 2012, ApJ, 753, 5
Rigby, J. R., Wuyts, E., Gladders, M. D., Sharon, K., & Becker, G. D. 2011, ApJ, 732, 59
Rodighiero, G., Daddi, E., Baronchelli, I., et al. 2011, ApJL, 739, L40
Rodríguez-Zaurín, J., Arribas, S., Monreal-Ibero, A., et al. 2011, A&A, 527, A60
Rozas, M., Richer, M. G., López, J. A., Relaño, M., & Beckman, J. E. 2006, A&A, 455, 539
Rubin, K. H. R., Weiner, B. J., Koo, D. C., et al. 2010, ApJ, 719, 1503
Rupke, D. S. N., Kewley, L. J., & Barnes, J. E. 2010a, ApJL, 710, L156
Rupke, D. S. N., Kewley, L. J., & Chien, L.-H. 2010b, ApJ, 723, 1255
Saitoh, T. R., Daisaka, H., Kokubo, E., et al. 2009, PASJ, 61, 481
Schlegel, D. J., Finkbeiner, D. P., & Davis, M. 1998, ApJ, 500, 525
Shapiro, K. L., Genzel, R., Quataert, E., et al. 2009, ApJ, 701, 955
Sharon, K., Gladders, M. D., Rigby, J. R., et al. 2012, ApJ, 746, 161
Shirazi, M., Vegetti, S., Nesvadba, N., et al. 2013, arXiv:1306.6282
Siana, B., Smail, I., Swinbank, A. M., et al. 2013, ApJ, 698, 1273
Siana, B., Teplitz, H. I., Chary, R.-R., Colbert, J., & Frayer, D. T. 2008, ApJ, 689, 59
Simcoe, R. A., Burgasser, A. J., Schechter, P. L., et al. 2013, PASP, 125, 270
Springel, V., Di Matteo, T., & Hernquist, L. 2005, ApJL, 620, L79
Steidel, C. C., Erb, D. K., Shapley, A. E., et al. 2010, ApJ, 717, 289
Storey, P. J., & Zeippen, C. J. 2000, MNRAS, 312, 813
Swinbank, A. M., Smail, I., Longmore, S., et al. 2010, Natur, 464, 733
Swinbank, A. M., Webb, T. M., Richard, J., et al. 2009, MNRAS, 400, 1121
Swinbank, M., Smail, I., Sobral, D., et al. 2012, ApJ, 760, 130
Tacconi, L. J., Genzel, R., Neri, R., et al. 2010, Natur, 463, 781
Tacconi, L. J., Neri, R., Genzel, R., et al. 2013, ApJ, 768, 74
Teyssier, R., Chapon, D., & Bournaud, F. 2010, ApJL, 720, L149
van Dam, M. A., Bouchez, A. H., Le Mignant, D., et al. 2006, PASP, 118, 310
van den Bergh, S., Abraham, R. G., Ellis, R. S., et al. 1996, AJ, 112, 359
Weiner, B. J., Coil, A. L., Prochaska, J. X., et al. 2009, ApJ, 692, 187
Whitmore, B. C., & Schweizer, F. 1995, AJ, 109, 960
Williams, R. J., Quadri, R. F., Franx, M., et al. 2010, ApJ, 713, 738
Wisnioski, E., Glazebrook, K., Blake, C., et al. 2011, MNRAS, 417, 2601
Wisnioski, E., Glazebrook, K., Blake, C., et al. 2012, MNRAS, 422, 3339
Wizinowich, P. L., Le Mignant, D., Bouchez, A. H., et al. 2006, PASP, 118, 297
Wuyts, E., Barrientos, L. F., Gladders, M. D., et al. 2010, ApJ, 724, 1182
Wuyts, E., Rigby, J. R., Gladders, M. D., et al. 2012a, ApJ, 745, 86
Wuyts, E., Rigby, J. R., Sharon, K., & Gladders, M. D. 2012b, ApJ, 755, 73
Wuyts, S., Förster Schreiber, N. M., Genzel, R., et al. 2012c, ApJ, 753, 114
Wuyts, S., Förster Schreiber, N. M., van der Wel, A., et al. 2011, ApJ, 742, 96
Yuan, T.-T., Kewley, L. J., Swinbank, A. M., & Richard, J. 2012, ApJ, 759, 66
Yuan, T.-T., Kewley, L. J., Swinbank, A. M., Richard, J., & Livermore, R. C. 2011, ApJL, 732, L14
Zaritsky, D., Kennicutt, R. C., Jr., & Huchra, J. P. 1994, ApJ, 420, 87